Preprints (www.preprints.org) | NOT PEER-REVIEWED | Posted: 6 July 2022 doi:10.20944/preprints202207.0083.v1

Brief Report

Screening Biophysical Sensors and Actuators that Influence Wound Healing in Human Induced Pluripotent Stem Cell-Derived Neurons

Vaibhav P. Pai[1], Ben Cooper[2] and Michael Levin[1*]

[1] Allen Discovery Center at Tufts University, Medford, MA, USA
[2] Department of Stem Cell and Regenerative Biology, Harvard University, Cambridge, MA 02138, USA
* Correspondence: Corresponding Author: Email: michael.levin@tufts.edu

Abstract:

All living cells maintain a charge distribution across their cell membrane (membrane potential) by carefully controlled ion fluxes. These bioelectric signals regulate cell behavior (such as migration, proliferation, differentiation) as well as higher-level tissue and organ patterning. Thus, voltage gradients represent an important parameter for diagnostics as well as a promising target for therapeutic interventions in birth defects, injury, and cancer. However, despite much progress in cell and molecular biology, little is known about bioelectric states in human stem cells. Here, we present simple methods to simultaneously track ion dynamics, membrane voltage, cell morphology, and cell activity (pH and ROS), using fluorescent reporter dyes in living human neurons derived from induced neural stem cells (hiNSC). We developed and tested functional protocols for manipulating ion fluxes, membrane potential, and cell activity, and tracking neural responses to wounding and re-innervation in vitro. Finally, using morphology sensor, we tested and quantified the ability of physiological actuators (neurotransmitters and pH) to manipulate nerve wound re-innervation. These methods are not specific to a particular cell type and should be broadly applicable to the study of bioelectrical controls across a wide range of combinations of models and endpoints.

Keywords: bioelectricity; ion flux; membrane potential; live sensor dyes; pH; serotonin; acetylcholine; GABA; hiNSC

Introduction:

Ion fluxes and membrane potential are fundamental aspects of biology and regulate cell behavior and function across species from plants and single cell organisms to vertebrates [1-10]. These ion fluxes and membrane potential mechanisms, along with biomechanical forces and canonical genetic-biochemical signals, regulate complex processes such as development, regeneration, wound healing, and disease states such as cancer [1,10-21]. Development of bioelectric interventions for regenerative medicine [22-24] requires an extensive database of physiological profiles of a wide range of cells, as well as methods for the study of the effects of bioelectric actuation on cell behavior. This especially concerns stem cells such as iPSCs and their derived tissues. However, few data on this are available, especially in human cells. Thus, we sought to develop

© 2022 by the author(s). Distributed under a Creative Commons CC BY license.

Preprints (www.preprints.org) | NOT PEER-REVIEWED | Posted: 6 July 2022 doi:10.20944/preprints202207.0083.v1

methods for reading and writing dynamic bioelectric states in cell culture. Here we report the results of testing a variety of reagents and protocols, resulting in simplified, robust methods for the use of live sensors simultaneously allowing characterization of cell morphology, ion dynamics, membrane potential, and cell activity such as changes in pH and reactive oxygen species during wounding and repair over time. We also show actuation of repair processes by bioelectric modulators (neurotransmitters and pH).

Wound repair is a highly complex set of events involving precise coordination between homeostasis, inflammation, proliferation, and remodeling [25,26]. Improper repair and healing results in numerous pathologies while perfect repair (no scarring) is seen in fetal tissues and many organisms that show full regeneration [26-29]. Thus, understanding wound repair not only holds the promise of remedying ailments such as chronic wounds but also gain insights for triggering latent regenerative abilities of tissues. Ion fluxes [30-32] and membrane potential [33-38] are critical regulators of wound healing and regeneration [1,20,39-44].Nerve regeneration in wounds is also considered important for faster and better (less scaring) [45-50], wound healing with neurite outgrowth into the wound often used as a good measure of neuronal regeneration [45,50-56]. There is also significant evidence for ion flux and membrane potential mediated effect on innervation into wounds [54,57-59]. Thus, we sought to develop protocols for testing bioelectric sensors and actuators on wounds made in cultured neural tissues. We report tracking ion fluxes and membrane potential as well as neuronal wounding and subsequent neurite outgrowth over time. We also test biophysical actuators (pH and neurotransmitters) for modulating the neurite outgrowth post wounding.

Human induced Neural Stem Cells (hiNSC) derived neurons have unique advantages over both commercially available transformed neuronal cells (such as PC12 and neuroblastoma) and primary human neural cells. The commercial neural cell lines are transformed, resulting in lack of complete neuronal functionality and poor differentiation leading to low predictivity and less reliable results [60-62]. On the other hand, primary human neural cells involve ethical limitations, require extensive resources and techniques, and are difficult to obtain on a consistent basis [63,64]. In contrast, hiNSC-derived neurons have function and behavior similar to primary neurons and are easy to culture in large quantities on a consistent manner [65-70]. Additionally, hiNSCs can be driven to represent both central and peripheral neurons making them highly versatile [65,66,70]. Hence in this study we use these hiNSC derived neurons.

Here we set up a culture of hiNSC derived mature neurons, in which we screened several live biophysical sensors to assess properties of living neural cells and culture generally falling into three categories a) Cell morphology, b) Ion fluxes and membrane potential, and c) Cell activity (as indicated by changes in pH and reactive oxygen species levels). We then use some of these sensors to track and quantify wound healing in these neuronal culture over time. Finally, we use some actuators (neurotransmitters and changes in pH) to test their effects on neurite outgrowth and healing over time and show that nerve wound repair and regeneration

Preprints (www.preprints.org) | NOT PEER-REVIEWED | Posted: 6 July 2022 doi:10.20944/preprints202207.0083.v1

can be modulated. These protocols and characterization data may facilitate similar approaches in a wide range of models.

Materials and Methods:

Cell culture

hiNSC were a generous gift from Dr. David Kaplan, Tufts University and cultured as per the previously established protocol [65]. Briefly, hiNSC cells were plated on mouse embryonic fibroblast (MEF) (obtained from ATCC) feeder layers that were previously inactivated with mitomycin C (Sigma), in hiNSC media: knockout (KO) Dulbecco's Modified Eagle's Medium (DMEM) (Thermo Fisher) supplemented with 20% KO xeno-free SR (Thermo Fisher), 20 ng/ml recombinant bFGF (Thermo Fisher), 1% Glutmax (Thermo Fisher), 1% antibiotic-antimycotic (Thermo Fisher), and 0.1mM β-mercaptoethanol (Thermo Fisher). Media was changed every 1-3 days. For hiNSC differentiation into mature neurons, hiNSC growing on inactivated MEF feeder layer were trysinized (TrypLE Select – Thermo Fisher) and resuspended in differentiation media: Neurobasal (Thermo Fisher) media supplemented with 2% B27 (Thermo Fisher), 1% Glutmax, and 1% antibiotic-antimycotic. Using manual pipetting and vortexing cell clumps and colonies were dissociated into single cell suspension, passed through 40-70µM cell strainer and plated on cell culture surface coated with poly-D-Lysine (Thermo Fisher) and Laminin (Thermo Fisher) in the differentiation media. Media was changed every 2 days or as needed.

Live sensor dyes

All live sensor dye tests were done on hiNSC derived day 10 mature neurons grown in 96 well culture plates coated with PDL+laminin. Each experiment was done in triplicates for each condition and the experiment was repeated at least 3 times. Cell morphology dyes: Calcein-Green AM (Thermo Fisher) (tested - 0.5-10µM, final 0.5µM), and Calcein Red-Orange AM (Thermo Fisher) (final 0.5µM), NeuO (StemCell Technologies) (tested 0.1-0.3µM, final 0.3µM), were mixed into the culture media and cells were incubated in the dye for 30 mins (Calcein dyes) or 60 mins (Neuo) followed by wash with media followed by fluorescence imaging: Calcein-Green AM (ex/em–494/517nm), Calcein Red-Orange AM (ex/em-577/590nm) and NeuO (ex/em-470/555nm). Nuclear dyes: DAPI (Sigma-Aldrich) (tested 0.5-10µgs/ml, final 0.5µgs/ml), Hoechst (Thermo Fisher) (tested 0.5-10µgs/ml, final 0.5µgs/ml) were mixed into the culture media and added onto the cells and incubated for 5 mins then dye was removed by 3 washes with media followed by fluorescence imaging: DAPI (ex/em-358/461nm) and Hoechst (ex/em-350/470nm). Ion flux and membrane voltage dyes: Intracellular Na^+ dye, CoroNa Green AM (Thermo Fisher) (tested 0.5-12.5µM, final 12.5µM), intracellular K+ dye, Asante Potassium Green – APG2 AM (Abcam) (tested 1-5µM, final 5µM), intracellular Cl- dye MQAE (Thermo Fisher) (tested 0.1-10µM, final-none worked), intracellular Ca2+ dye Fluo4 AM

Preprints (www.preprints.org) | NOT PEER-REVIEWED | Posted: 6 July 2022 doi:10.20944/preprints202207.0083.v1

(Thermo Fisher) (tested 1-5µM, final 5µM), and membrane potential dye DiBAC (Thermo Fisher) (tested 1-12.5µM, final 5.5µM) were mixed into the culture media and cells were incubated in the dye for 60 mins followed by two washes with media then incubation in regular media or custom Tyrode solutions for 10 mins followed by fluorescence imaging: CoroNa Green AM (ex/em-492/516nm), APG2 AM (ex/em-488/546nm), MQAE (ex/em-350/460nm), Fluo4 AM (ex/em-494/516nm), and DiBAC (ex/em-419/516nm). Cell activity dyes: Intracellular reactive oxygen species dye Peroxy Orange 1 (PO1) (R&D Systems) (tested 1-5µM, final 5µM) was mixed with media and cells were incubated in the dye for 60 mins. 30 mins into the incubation period 500µM H2O2 was added to the media. At the end of 60 min incubation the cells were washed twice with media followed by fluorescent imaging (ex/em-543/565nm). Intracellular pH dye SNARF-5F AM (Thermo Fisher) (tested 5-20µM, final 5µM) was mixed in media (serum free) and cells were incubated in the dye for 30 mins followed by media washes and incubation in media with varying pH (6-8) with or without protonophore compound CCCP (hellobio) (5µM) for 10 mins followed by fluorescence imaging (ex-488-530nm, em-580nm and 640nm). Due to ratiometric nature of the dye ratio of intensities (640nm/580nm) was obtained using Fiji software for pH analysis. All imaging was done using EVOS M7000 System (Thermo Fisher)

Immunostaining

Briefly, hiNSC were grown in coated 96 well culture plates, fixed in 4% parafolmaldyhyde, washed 3 times in 1X phosphate-buffered saline (PBS), blocked in PBS with 10% goat serum and 0.1% triton X-100. for 1 hour at room temperature (RT), incubated in primary antibody diluted in blocking buffer overnight at 4°C, following day rinse in PBS 4 times and incubate in corresponding fluorescently conjugated secondary antibody in blocking buffer for 1 hour at RT protected from light, counterstain nuclei with DAPI or Hoechst for 5 mins at RT. Primary antibodies used were rabbit anti-beta III tubulin (TUJ1) 1:500 (abcam-ab18207), rabbit anti- Choline acetyl transferase (ChAT) 1:500 (Thermo Fisher-50-173-3063), rabbit anti-serotonin reuptake transporter (SERT) 1:500 (abcam-ab272912), and rabbit anti- glutamate decarboxylase 67 (GAD67) 1:500 (Thermo Fisher-PA5-21397). Secondary antibody used was goat anti-rabbit Alexa 488 conjugated 1:1000 (Thermo Fisher-A-11070). Imaging was done using EVOS M7000 System (Thermo Fisher).

Scratch assay

All scratch assays were done on hiNSC derived day 10 mature neurons grown in 96 well culture plates coated with PDL+laminin. Each experiment was done in triplicates for each condition and the whole experiment was repeated at least 3 times. Day 10 mature neurons were scratch wounded mechanically using a sterile P10 pipette tip, washed with media and incubated in fresh media, media with varying pH, or media with indicated concentrations of acetylcholine, serotonin, or GABA for 48 hours followed by washing with

Preprints (www.preprints.org) | NOT PEER-REVIEWED | Posted: 6 July 2022 doi:10.20944/preprints202207.0083.v1

fresh media and incubation in fresh media for the rest of experimental duration. Cells were stained with Calcein AM dye at the mentioned time points and imaged using EVOS M7000 System (Thermo Fisher).

Neurite density quantification

Scratch wounds stained with Calcein Red-Orange AM were used. Three random images of the scratch wound were captured from each well of the 96 well plate for reach replicate of each experiment. Using Fiji software, the images were adjusted to a color threshold and binarized. A fixed region of interest marking the same wound region was used to calculate integrated density. Neurite density was calculated as integrated density/area.

Statistics:

Statistical analyses were performed using GraphPad Prism9. At least three technical replicates and at least three independent experiments were used for analysis per experimental condition. Data were analyzed by ANOVA (for more than two groups, with Tukey's multiple comparison test) or as indicated with each experiment. A p-value less than 0.05 was considered significant. Data are represented as mean $\pm$SD.

Preprints (www.preprints.org) | NOT PEER-REVIEWED | Posted: 6 July 2022 doi:10.20944/preprints202207.0083.v1

Results & Discussion:

Establishing human induced neural stem cell (hiNSC) derived neuron cultures.

We began by characterizing hiNSC growth *in vitro* [65-70]. hiNSC cells propagated on inactivated mouse embryonic fibroblasts (MEFs) (Figure 1A) were resuspended and plated on poly-D-Lysine (PDL) and Laminin coated wells of 96 well plates with differentiation media (Figure 1B-D). Cells were fixed and stained at regular intervals (day 1, 4, 7, 10, 15) for mature neuron marker TUJ1(βIII tubulin) and nuclear marker DAPI (Figure 1E-F). We observed that the TUJ1 positive mature neurons (seen as long green neuronal projections) started to appear slowly starting day 4 (Figure 1F). By day 10 majority of cells stain TUJ1 positive (Figure 1H) and by day 15 they form extensive neural networks (Figure 1I). We concluded that our cultures reach neuronal cell maturity by day 10, and thus used day 10 neuronal cultures for further experimentation. Since these cells can be grown in 96 or 384 well plates they are amenable for high throughput screens and assays which can be combined with high-content large-field of view image acquisition and analysis [71] to create a real-time screening protocol.

Preprints (www.preprints.org) | NOT PEER-REVIEWED | Posted: 6 July 2022 doi:10.20944/preprints202207.0083.v1

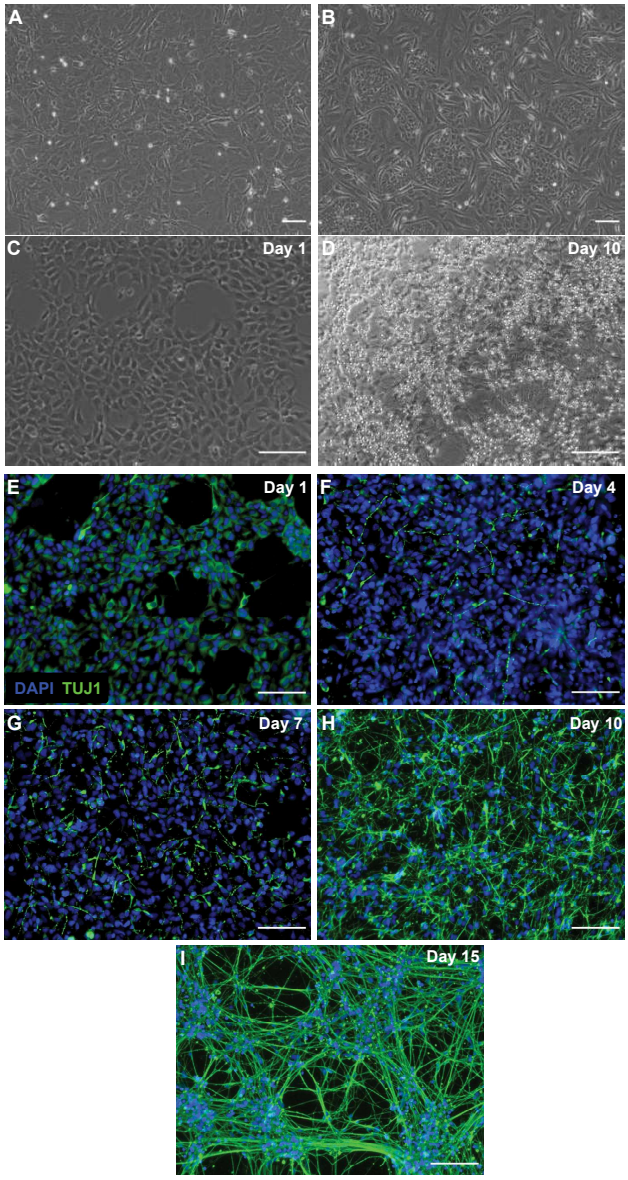

Figure 1: hiNSC differentiation into mature neurons over 10 days
(A) inactivated MEFs which serve as feeder substrate for growing hiNSCs. (B) hiNSC colonies growing on inactivated MEFs. (C) Day 1 after seeding hiNSCs on tissue culture surface coated with Poly D-Lysine (PDL)+laminin. (D) Day 10 after seeding hiNSCs on PDL+laminin with mature neuronal outgrowths. (E) Day 1 hiNSCs on PDL+laminin stained with DAPI (nucleus) and immunostained with TUJ1 (neuron-specific βIII-tubulin) showing no mature neurons. (F) Day 4 hiNSCs on PDL+laminin stained with DAPI and TUJ1 showing beginning of neuronal differentiation. (G) Day 7 hiNSCs on PDL+ laminin stained with DAPI and TUJ1 showing increased progression of neuronal differentiation. (H) Day 10 hiNSCs on PDL+laminin stained with DAPI and TUJ1 showing large-scale neuronal differentiation into mature neurons. (I) Day 10 hiNSCs on PDL+laminin stained with DAPI and TUJ1 showing extensive neural networks. All scale bars, 100 µm.

Live sensors for detecting healthy neurons and their morphology in hiNSC derived neurons.

Ability to assess the viability and morphology of live neurons (without affecting neuronal health) is vital in determining their health, changes in morphology under various conditions and detect neurite outgrowth patterns during processes such as wound healing. Our dye testing results are summarized in Table 1.

Preprints (www.preprints.org) | NOT PEER-REVIEWED | Posted: 6 July 2022 doi:10.20944/preprints202207.0083.v1

Table 1: List of biophysical dyes and their outcome with hiNSC derived neurons

	Sensor Dye	Purpose	Live/Endpoint	Works/Does not work
Morphology	DAPI	Nuclear stain	Endpoint	✓
	Hoechst	Nuclear stain	Endpoint	✓
	NeuO	Cell morphology	Live stain	✗
	Calcein AM - Green	Cell morpholgy	Live stain	✓
	Calcein AM - Red	Cell morphology	Live stain	✓
V_{mem} & ion flux	DiBac	Membrane voltage	Live stain	✓
	CoroNA AM	Intracellular Na^+	Live stain	✓
	APG-2 AM	Intracellular K^+	Live stain	✓
	Fluo4 AM	Intracellular Ca^{2+}	Live stain	✓
	MQAE	Intracellular Cl^-	Live stain	✗
Cell activity	SNARF-5F AM	Intracellular pH	Live stain	✓
	PO1	Intracellular ROS	Live stain	✓
	2-NBDG	Glucose uptake	Live stain	✗

We first tested whether nuclear stains could be used while maintaining viable neurons. We tested multiple concentrations of DAPI (0.5-10µgs/ml); however, DAPI-staining heavily favored dead cells at all concentrations, with no live cell staining detectable even at 0.5µgs/ml (Figure 2A) and DAPI exposure itself was toxic to the neurons inducing cell death. At concentrations lower than 0.5µgs/ml, DAPI stained neither dead nor live cell nuclei. We then tested Hoechst nuclear stain (0.5-5µgs/ml) [72,73]. At low concentration (0.5µgs/ml), Hoechst showed graded staining with live neurons showing lightly stained nuclei and dead cells showing brightly stained nuclei (Figure 2B). Although Hoechst was better tolerated by neurons than DAPI, the neuron cultures still showed distress (blebbing, shorter neurites, rounded cell bodies and loosed attachment). In addition, the dye toxicity may be further amplified by short wavelength phototoxicity which could be avoided by use of red nuclear stains. Hence, these nuclear stains might be good sensor for counting neurons and nuclear morphology, but they are not well compatible with maintaining live cultures and are best used as end point assays.

Preprints (www.preprints.org) | NOT PEER-REVIEWED | Posted: 6 July 2022 doi:10.20944/preprints202207.0083.v1

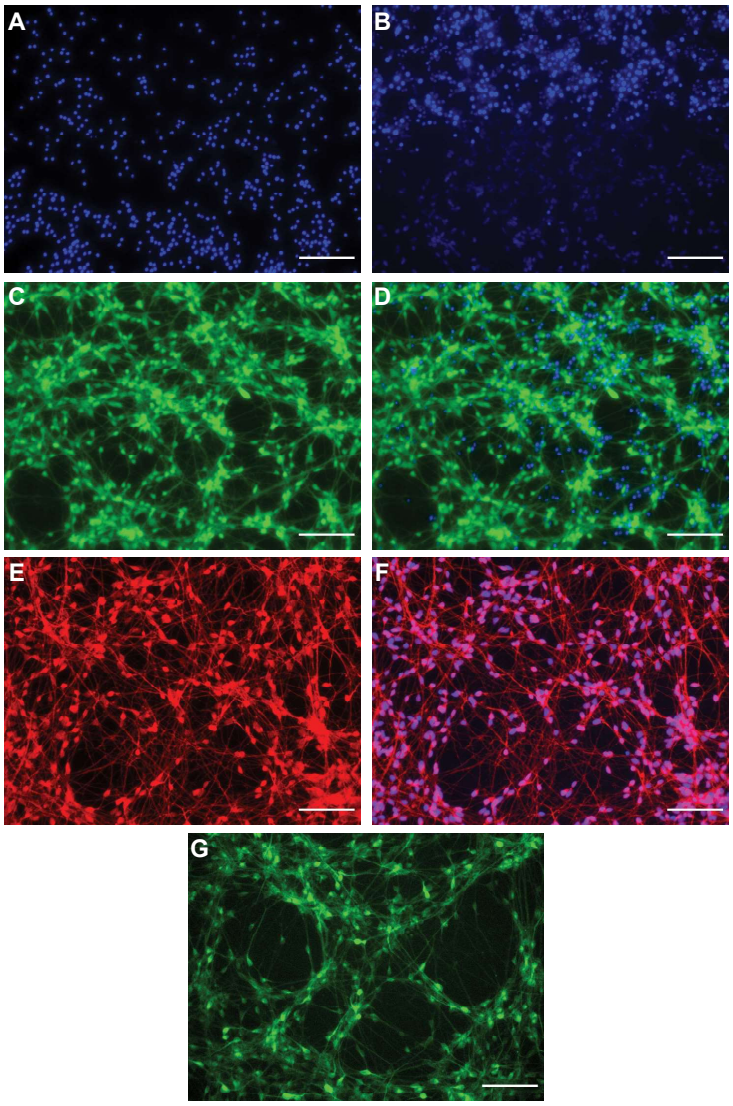

Figure 2: Screening live morphology dyes on hiNSC derived mature neurons
(A-G) hiNSC derived day 10 mature neurons. (A) Stained with 0.5 µg/ml DAPI showing only dead cells nuclei. (B) Stained with 0.5 µg/ml Hoechst showing top half (bright blue) dead cells nuclei and bottom half (light blue) live cells nuclei. (C) Stained with 0.5 µM Calcein Green AM showing live neurons cell body and axonal projections. (D) Stained with 0.5 µM Calcein Green AM and DAPI with green showing live neuron morphology and blue showing dead cells nuclei. (E) Stained with 0.5 µM Calcein Red-Orange AM showing live neurons cell body and axonal projections. (F) Stained with 0.5 µM Calcein Red-Orange AM and Hoechst with red/magenta showing live neuron morphology and blue showing live neuron nuclei. (G) Stained with 0.3 µM NeuO showing live neurons cell body and axonal projections. All scale bars, 100 µm.

To detect live neurons and see their overall morphology, we tested sensor CalceinAM-green (0.5-5µM). 0.5µM CalceinAM-green was sufficient to labeled live neurons and beautifully showed the overall morphology of neuronal cells (Figure 2C). The neurons remained healthy and brightly labeled up to 24 hours post exposure (Figure 2D). Therefore, we attempted to monitor the neuron morphologies over 24-hour period with time lapse imaging. However, we found repeated exposure to GFP wavelength (Ex-488nm, Em-524nm)

Preprints (www.preprints.org) | NOT PEER-REVIEWED | Posted: 6 July 2022 doi:10.20944/preprints202207.0083.v1

caused significant phototoxicity in the neurons. We then attempted to monitor and visualize the neuron morphologies over multiple days by exposing them to CalceinAM-green every 24 hours. However, repeated imaging and frequent exposure to CalceinAM-green also induced phototoxicity stress in the neurons under these conditions. Some of the stress could also be due to the frequent media changes and washes required for dye staining.

The frequency of exposure to CalceinAM-green that does not detrimentally affect the neurons was found to be 48 hours. Considering the phototoxicity issue, we tested another version CalceinAM-red-orange and found the red shifted wavelengths (Ex-540nm, Em-590nm) to be better tolerated by the neurons without any significant phototoxicity (Figure 2E & F). Lastly, we tried NeuO which is proposed to selectively label only neurons and indicate their viability and morphology. Among the concentrations tried (0.1-0.3µM), 0.3µM NeuO nicely labelled live neurons; however, majority of the signal was mostly perinuclear and less prominent in neuronal projections which did not indicate the morphology of the neurons very well (Figure 2G). Also, we found NeuO not to be selectively labelling neurons and labels other non-neural cells such as macrophages (Figure S1).

Overall, we conclude that CalceinAM-red-orange serves well for determining viability and morphology of neurons and for tracking their morphology over extended times without any detrimental impact on the health of neuronal cultures. NeuO can be used for detecting live neurons (but not their morphology) and where interest is in observing perinuclear region of neurons.

Live sensors for detecting changes in intracellular ion concentrations and resting membrane potential in hiNSC derived neurons.

Given the importance of bioelectrical cell-states for cellular behaviors *in vitro and in vivo* [1-10,15,16,42,43,74-83], we next focused on testing fluorescent sensors that could report ion and voltage dynamics. We sought protocols that enable tracking of parameters such as changes in ion levels and membrane potential in live neurons over spatio-temporal scales in response to stimuli, injury, regeneration, or environmental change, which would not be possible with canonical static patch clamp and voltage measurements techniques.

We first tested intracellular Na^+ ion sensor CoroNa-AM (tested 0.5-12.5µM and used 12.5µM for all experiments). CoroNa-AM enters the cells and exhibits an increase in fluorescence emission intensity upon binding Na^+ ions. Previously it has been shown to detect intracellular Na^+ in neurons within brain slices [84], and we used an established protocol for modulating extracellular Na^+ [85]. A completely defined Tyrode solution was used as a starting extracellular solution with physiological levels of ions (high extracellular Na^+ - 140mM in comparison to cytosol). In a stepwise manner over five solutions Na^+ ions were gradually replaced with impermeable N-Methyl-D-glucamine ($NMDG^+$) with K^+ concentration maintained at physiological levels (Table S1). This allows maintaining the osmolarity and electroneutrality to isolate the effect of Na+.

Preprints (www.preprints.org) | NOT PEER-REVIEWED | Posted: 6 July 2022 doi:10.20944/preprints202207.0083.v1

Modified Tyrode solutions with Na^+ concentration of 28mM, 56mM, 84mM, 112mM, and 140mM (physiological level) were used as extracellular solutions to test their effect on CoroNa-AM sensor signal. hiNSC derived day 10 mature neurons were stained with CoroNa-AM followed by incubation in the modified Tyrode solutions with varying extracellular Na^+ ions. We observed a significant (ANOVA, $p<0.0001$) dose dependent increase in CoroNa-AM signal (indicating increase in intracellular Na^+) in relation to increase in extracellular Na^+ (Figure 3A). Thus, CoroNa-AM successfully detects intracellular Na^+ ion changes in live neurons and can be used to study intracellular Na^+ ion dynamics of neurons in response to various stimuli, injury, regeneration, and other extracellular environmental changes.

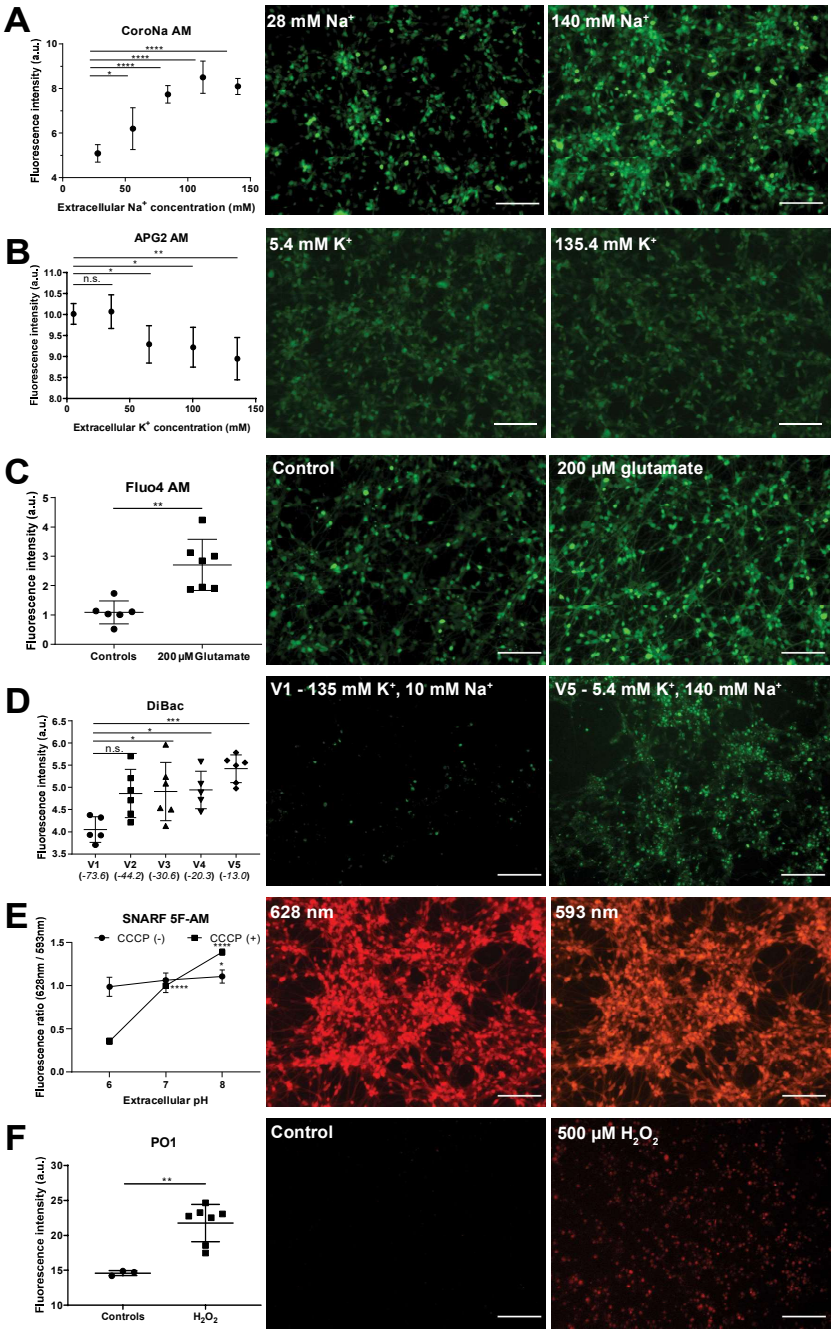

Preprints (www.preprints.org) | NOT PEER-REVIEWED | Posted: 6 July 2022 doi:10.20944/preprints202207.0083.v1

Figure 3: Screening live biophysical dyes showing dynamics of ions, Vmem, pH, and metabolism in hiNSC derived mature neurons
(A-F) hiNSC derived day 10 mature neurons. (A) CoroNA AM fluorescent intensity plot showing increase in intracellular Na^+ ions in response to increasing extracellular Na^+ ion concentrations. Representative images of CoroNa AM stained cells incubated in 28 mM and 140 mM extracellular Na^+ ion concentration. (B) APG2 AM fluorescent intensity plot showing decrease in intracellular K^+ ions in response to increasing extracellular K^+ ion concentrations. Representative images of APG2 AM stained cells incubated in 5.4 mM and 135.4 mM extracellular K^+ ion concentration. (C) Fluo4 AM fluorescent intensity plot showing increased intracellular Ca^{2+} ions in response to 200µM glutamate. Representative images of Fluo4 AM stained cells in control and 200µM glutamate conditions. (D) DiBac fluorescent intensity plot showing increase in resting membrane voltage of cells in response to changing extracellular ion concentrations. Representative images of DiBac stained cells in V1 (135 mM K^+, and 10 mM Na^+) and V5 (5.4 mM K^+, and 140 mM Na^+) extracellular solutions. (E) SNARF 5F AM fluorescence ratios (628nm/593nm) showing no change in intracellular pH in absence of protonophore CCCP but a significant change in intracellular pH in presence of protonophore CCCP (50 µM) in response to extracellular pH changes. Representative images of SNARF 5F AM at 628nm and 593nm for extracellular pH 7. (F) Peroxy Orange 1 (PO1) fluorescent intensity plot showing increase in intracellular reactive oxygen species (ROS) in response to hydrogen peroxide treatment. Representative images of PO1 stained cells in control and 500 µM hydrogen peroxide conditions. All data are represented as mean±S.D. All scale bars, 100 µm.

We next used Asante Potassium Green-2-AM (APG2-AM) (tested 1-5µM and used 5µM for all experiments) to monitor intracellular K^+ ion dynamics of the hiNSC derived neurons. APG2-AM also enters cells and exhibits increase in fluorescence intensity upon binding K^+ ions. To study the dynamics of K^+ ions, we again used modified Tyrode solutions [85]. Physiologically extracellular K^+ ions are low (5.4mM) in comparison to cytosol. Here, over the five solutions we slowly increased extracellular K^+ ions with a corresponding decrease in NMDG (Table S2). Here NMDG was used to substitute for Na^+ to keep osmolarity constant while solely modulating K^+. Modified Tyrode solutions with K^+ concentrations of 5.4mM (physiological level), 35.4mM, 65.4mM, 100.4mM, and 135.4mM were used as extracellular solutions. hiNSC derived mature neurons were stained with APG2-AM followed by incubation in the modified Tyrode solutions with varying extracellular K^+ ions. As expected, we observed a significant (ANOVA, $p<0.001$) dose-dependent decrease in APG2-AM signal (indicating decreasing intracellular K^+ ions) in relation to increase in extracellular K^+ (Figure 3B). Although significant (ANOVA, $p<0.001$) the decrease in APG2-AM signal was not as pronounced as expected. This might be because, although APG2-AM is sensitive to K^+ ions, recently it has been shown to also be sensitive to other cations particularly Na^+ [86]. Hence, the intracellular Na^+ dynamics might still dampen the effect of APG2-AM. A newer APG4-AM sensor has been shown to have much high sensitivity to K^+ compared to other cations and might be better for a finer analysis of intracellular K^+ dynamics. Nonetheless, APG2-AM successfully detects intracellular K^+ ion changes in live neurons and can thus be used to study intracellular K^+ ion dynamics in neurons in response to various stimuli, injury, regeneration, and other extracellular environmental changes.

Preprints (www.preprints.org) | NOT PEER-REVIEWED | Posted: 6 July 2022 doi:10.20944/preprints202207.0083.v1

Because anions are an important and highly tractable bioelectric control point [87,88], we next sought to use MQAE sensor to detect intracellular Cl^- ion dynamics within hiNSC derived neurons. MQAE has been previously used to detect intracellular Cl^- ion dynamics in neurons [89-91]. MQAE signal intensity is inversely proportional to intracellular Cl^- ions. Unfortunately, after trying various concentrations of the MQAE sensor (0.1 – 10mM) we were unable to detect any discernable signal above the background in the hiNSC derived neurons (Figure S2). The majority of studies successfully employing MQAE use a two-photon microscope set up detecting MQAE via fluorescence lifetime imaging (FLIM) [89-91] as opposed to conventional fluorescent microscopy used in our setup. Perhaps use of such a FLIM imaging and analysis might allow use of MQAE in detecting intracellular Cl^- dynamics in the hiNSC derived neurons. Further investigation of use of MQAE using such a FLIM setup is warranted.

We then tested the Fluo4-AM sensor (tested 1-5µM and used 5µM for all experiments) to detect intracellular Ca^{2+} dynamics in hiNSC derived neurons. In many cases Ca^{2+} dynamics has been used as an indirect account of changes in membrane potential of neurons [92]. Neurons showed beautiful intracellular Ca^{2+} staining as well as baseline spiking dynamics of intracellular Ca^{2+} (Figure 3C & movie S1). However, we did notice discernable photoactivation of intracellular Ca^{2+} dynamics in neurons while taking movies (Movie S1). This suggests that repeated exposure to Fluo4-AM excitation wavelength (494nm) changes the baseline intracellular Ca^{2+} dynamics which should be carefully considered during experimentation. Glutamate is a potent inducer of free intracellular Ca^{2+} in neurons [93,94]. Incubating hiNSC derived neurons in 200µM glutamate for 10 mins resulted in a significant (t-test, $p<0.01$) and sustained increase in Fluo4-AM signal (Figure 3C) indicating a significant and sustained increase in intracellular Ca^{2+}. Thus, Fluo4-AM successfully detects intracellular Ca^{2+} ion changes in live neurons and can thus be used to study intracellular Ca^{2+} ion dynamics in neurons in response to various stimuli, injury, regeneration, and other extracellular environmental changes in addition to using it as a surrogate for membrane voltage changes.

Although intracellular Ca^{2+} dynamics have been used as an indirect indicator of membrane voltage change [92,95-97], there is not always a direct correlation between the two as Ca^{2+} also serves as a secondary messenger for multiple cellular signaling pathways [95,98,99], while transduction pathways other than Ca^{2+} can operate downstream of voltage change [1]. Most importantly, while fast-response dyes such as calcium dyes are ideal for characterizing spiking, the slowly-changing resting potential states critical for control of proliferation and differentiation are best visualized with slow response dyes. Here we use the DiBAC [100,101] voltage reporter dye (tested 1-12.5µM and used 5.5µM for all experiments) for a direct measurement of resting membrane potential of hiNSC derived neurons. As the cells depolarize (increase in resting membrane potential) DiBAC fluorescence increases {Yamada, 2001, 11488436}. To induce changes in resting membrane potential of neurons, we again used modified Tyrode solutions for extracellular conditions [85].

Preprints (www.preprints.org) | NOT PEER-REVIEWED | Posted: 6 July 2022 doi:10.20944/preprints202207.0083.v1

Using five solutions, we gradually increased K^+ and decreased Na+ (Table S3). This strategy has been shown to progressively increase the resting membrane potential of cells [85]. Using the Goldman-Hodgkin-Katz equation the membrane potential for the five solutions were calculated (-73.6mV, -44.2mV, -30.6mV, -20.3mV, and -13mV). hiNSC derived neurons were stained with DiBAC followed by incubation in the modified Tyrode solutions for 10mins. As expected, we observed a significant increase in DiBAC signal (suggesting depolarization) in relation to depolarizing extracellular solutions (Figure 3D). Thus, DiBAC successfully detects resting membrane potential changes in live neurons and can be used to study resting potential dynamics of neurons in response to various stimuli, injury, regeneration, and other extracellular environmental changes. Also, resting membrane potential changes can be visualized in combination with intracellular Ca^{2+}.

Thus, overall ion and membrane voltage sensors can be used for monitoring bioelectric parameters in live neurons. These sensors can also be used independently or in combination, for example, membrane voltage and intracellular Ca^{2+} can be monitored simultaneously to tease apart the independent and/or overlapping roles of the two during any event [98]. In addition, it can be concluded that the modified Tyrode solutions can be used as actuators to bring about a particular change in the bioelectric parameter to investigate role of specific ions or membrane potential in cellular phenomenon.

Live sensors for detecting changes in cellular state such as pH and metabolism in hiNSC derived neurons.

Intracellular pH is tightly linked to the excitability of neurons due to its effect on ion channels [102,103]. Electrical activity can lead to rapid changes in pH making mechanisms that regulate pH very important. As a result, intracellular pH is an important determinant of both physiological and pathophysiological conditions of neurons [102,103]. Also, environments like wounds have a very dynamic pH which in turn might affect intracellular pH [104-107]. Hence monitoring intracellular pH in neurons is important to characterize neuronal health and function. To monitor intracellular pH of hiNSC derived neurons we used the SNARF-5F-AM sensor (tested 5-20µM and used 5µM for all experiments). SNARF-5F-AM allows ratiometric measurement of fluorescence at two wavelengths (640nm/580nm) allowing quantitative determination of intracellular pH. hiNSC neurons stained with SNARF-5F-AM showed nice fluorescent signal at both wavelengths. To test the sensor, we prepared media with three different pH (pH 6, 7, and 8). After incubating the neurons in media with different pH for 10 mins, we saw a small but significant increase in ratio from pH 6 – 8 (Figure 3E). This observation is particularly interesting because generally cells are impermeable to protons (H+) and thus largely shield their intracellular pH from extracellular proton changes. Hence, it appears that the SNARF-5F-AM sensor is sensitive enough to detect even minor changes in intracellular pH. To further test the sensitivity of SNARF-5F-AM, we used a protonophore CCCP (5µM) along with media ranging in pH 6-8. This would allow transfer of protons between extracellular and intracellular solutions, thus forcing a change in intracellular pH

Preprints (www.preprints.org) | NOT PEER-REVIEWED | Posted: 6 July 2022 doi:10.20944/preprints202207.0083.v1

of neurons. Under these conditions we observed a large and significant increase in fluorescence ration from pH6-8 (Figure 3E). Thus, SNARF-5F-AM successfully detects changes in intracellular pH in live neurons and can be used to monitor intracellular pH of neurons while testing various conditions of stimuli, injury, regeneration, and other environmental changes. Changing extracellular pH can be used as a modality for changing intracellular pH of neurons albeit to a very small extent.

Neurons are metabolically active cells and reactive oxygen species (ROS) are largely byproducts of cellular metabolism [108-110]. Baseline levels of ROS are important in neurons for regulating signaling involved in differentiation, polarization, and synaptic plasticity while, excessive ROS accumulation results in oxidative damage to neurons [108-110]. Hence monitoring intracellular ROS in neurons is important to determine neuronal health. To monitor intracellular reactive oxygen species (ROS) in hiNSC derived neurons we used Peroxy Orange 1 (PO1) sensor (tested 1-5µM and used 5µM for all experiments) [111]. Once inside the cell, PO1 responds to ROS and emits fluorescence with intensity proportional to intracellular ROS. To test the sensor, we use media with 500µM hydrogen peroxide (H2O2). After incubating the neurons in media with H2O2 for 10 mins we observed a significant increase in PO1 signal (Figure 3F). Thus, PO1 successfully detects change in intracellular ROS in live neurons and can be used to monitor metabolic health of neurons under various conditions of stimuli, injury, regeneration and other environmental changes.

Overall, the pH and ROS sensors can be used to monitor the cell state in live neurons. These sensors can be used in any combination with the morphology dyes and the bioelectric sensors to monitor neuronal dynamics based on specific experimental variables. All together, the panel of morphology, bioelectric, and cell state sensors characterized above serve as powerful tools for monitoring intracellular biophysical dynamics in live neurons.

Establishing scratch assay for neuronal wounding and quantitative determination of neurite outgrowth from injured neurons using hiNSC derived neurons.

Wounding involves nerve injury in addition to many other aspects and neuronal regeneration and neurite outgrowth is an important determinant of proper wound healing [45,50-54,112]. Wound healing (scratch) assays are routinely performed to study injury and subsequent recovery [56]; thus we sought to establish methods to characterize bioelectric states during this process. Confluent hiNSCs differentiated into mature neurons over ten days were subjected to mechanical scratching (Figure 4A). The scratch location was monitored and imaged till day 11 post-scratch (Figure 4A-F). On day 1 post-scratch sparse small projections are given out into the scratch by neurons lining the scratch (Figure 4B). By day 4 post-scratch we observed that the small projections had grown into small, localized network of neurite outgrowths in the scratch connecting neighboring neurons (Figure 4C). By day 8 post-scratch they had grown into large neurite networks within the scratch with thick neurite fibers traversing across the scratch wound (Figure 4D). By day 11 post-

Preprints (www.preprints.org) | NOT PEER-REVIEWED | Posted: 6 July 2022 doi:10.20944/preprints202207.0083.v1

scratch it had grown into an extensive dense network of nerite outgrowth and thick neurite fibers covering the entire scratch wound (Figure 4E). Live morphology sensor Calcein Green-AM showed that these neurons, neurite networks, and fibers were live and healthy (Figure 4E). Given the technical problems with multi-day repeated use of Calcein Green-AM as discussed above, we used the well-tolerated Calcein Red-Orange-AM over ten days post-scratch to track and quantify neurite outgrowth (Figure 4G-I). We observed a marked increase in neurite density within the scratch wound between day 2 and day 10 post-scratch. This scratch wound assay and neurite density quantification was used to test effect of various stimuli on neuronal regeneration and recovery post-wounding.

Preprints (www.preprints.org) | NOT PEER-REVIEWED | Posted: 6 July 2022 doi:10.20944/preprints202207.0083.v1

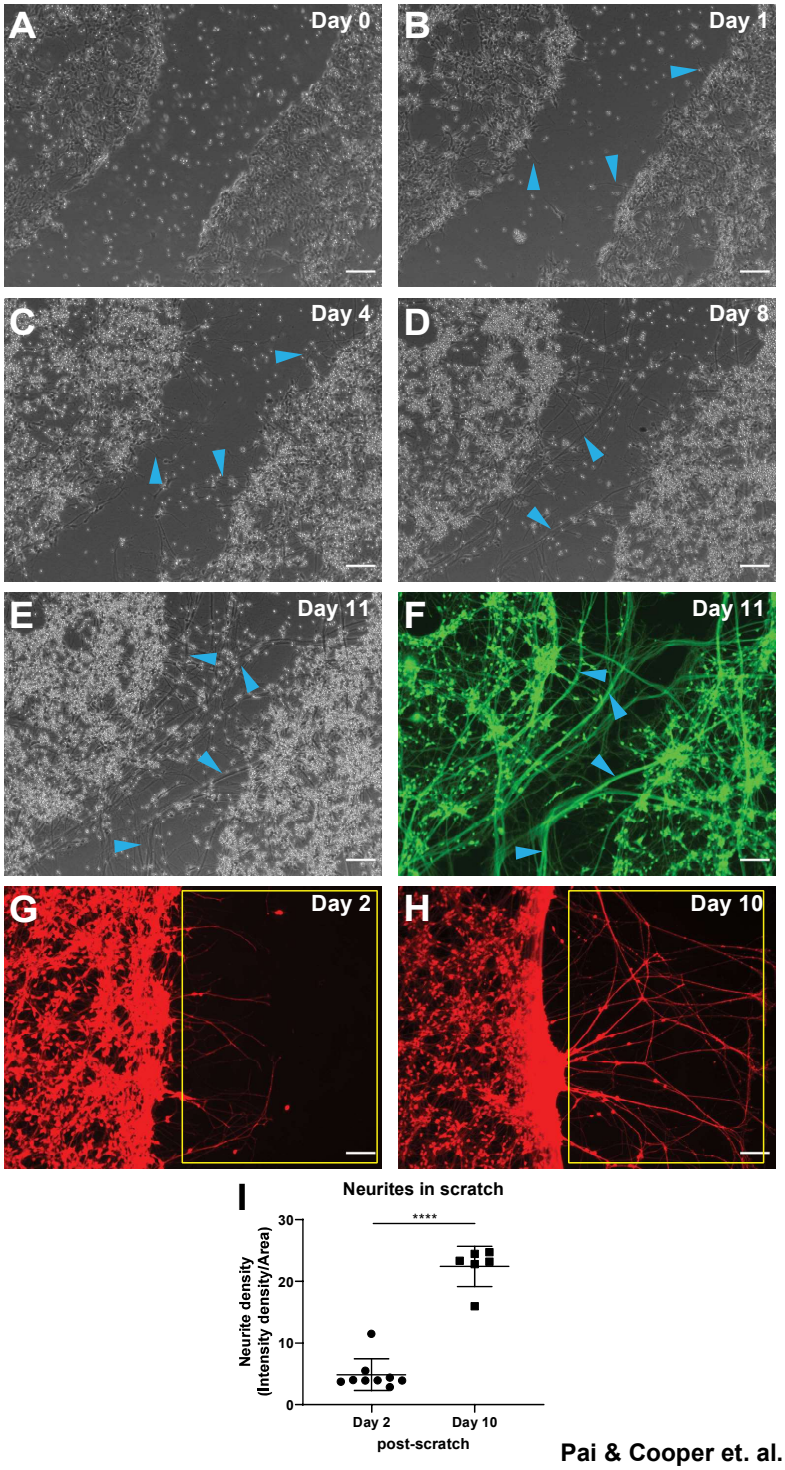

Figure 4: Scratch assay for neuronal wounding and quantitative determination of neurite outgrowth from injured mature neurons

(A) hiNSC derived day 10 mature neurons with a scratch wound. (B) Day 1 post-scratch sparse rudimentary outgrowth by some cells into the scratch wound are seen (blue arrowheads). (C) Day 4 post-scratch shows small, localized network of outgrowths between close neighboring cells within the scratch wound (blue arrowheads). (D) Day 8 post-scratch, large thick neural networks and neural fibers are seen throughout the scratch wound (blue arrowheads). (E) Day 11 post-scratch, the entire scratch wound is covered with neural

Preprints (www.preprints.org) | NOT PEER-REVIEWED | Posted: 6 July 2022 doi:10.20944/preprints202207.0083.v1

network and thick neural bundles can be observed traversing across the scratch wound (blue arrowheads). (F) Calcein Green AM live stain on day 11 post-scratch shows live neurons with extensive neurite outgrowth and nerve fibers throughout the scratch wound. (G-H) Calcein Red-Orange AM live staining of day 2 post-scratch (G) and day 10 post-scratch (H) for quantifying overall neurite outgrowth. Yellow box indicates the region of interest for measuring neurite outgrowth as intensity density. (I) hiNSC derived mature neurons show a significant increase in neurite density between day 2 and day 10 post-scratch. All data are represented as mean±S.D. All scale bars, 100 µm.

Acetylcholine has biphasic effect on neurite outgrowth after scratch wound.

Neurotransmitter signaling is both a canonical transduction step downstream, and a trigger upstream, of voltage dynamics, not only in neurons but also in non-neural cells [113-116]. Much work has gone into serotonergic endpoints in bioelectric signaling [117-119], but the effects of neurotransmitters on repair by hiNSC derivatives are largely unknown. Thus, we used our system to examine functional impacts of a number of neurotransmitters, starting with acetylcholine, which is known to affect the central and peripheral nervous system as well as non-neural tissues through its ionotropic (direct influence on membrane voltage) and metabotropic (complex long term effects) receptors [120,121].

To test the effect of acetylcholine on neurite outgrowths after wounding, we first checked if hiNSC derived mature neurons have cholinergic neurons. Immunostaining for choline acetyl transferase showed cholinergic neurons distributed evenly throughout cultures (Figure 5A). Neurons were then mechanically wounded as mentioned above and left untreated (controls) or treated with three different concentrations of acetylcholine (250µM, 500µM, 1mM) for 2 days. On day 2 post-scratch the 250µM and 500µM acetylcholine treated scratch wounds were indistinguishable from controls (Figure 5B). However, 1mM acetylcholine significantly reduced the number of neurite outgrowth and neurite density (Figure 5B-D). Contrarily, day 10-post-scratch showed a significant increase (in comparison to controls) in overall neurite density in acetylcholine treatment which peaks at 500µM and then fall back a bit in 1mM (Figure 5E-G). Although the increase in neurite density is striking (Figure 5F & G), we observed this increase mainly in the number of neurite fibers running parallel to the scratch wound. The neurite outgrowths away from the scratch surface (perpendicular to scratch) were the same if not reduced in comparison to controls (Figure 5F & G). Thus, acetylcholine seems to show a biphasic effect on neurite outgrowth with suppression of neurite outgrowth on day 2 post-scratch but an enhanced neurite density by day 10 post-scratch with neurite fibers mainly arranged parallel to wound, a sign of detrimental nerve and wound repair.

Preprints (www.preprints.org) | NOT PEER-REVIEWED | Posted: 6 July 2022 doi:10.20944/preprints202207.0083.v1

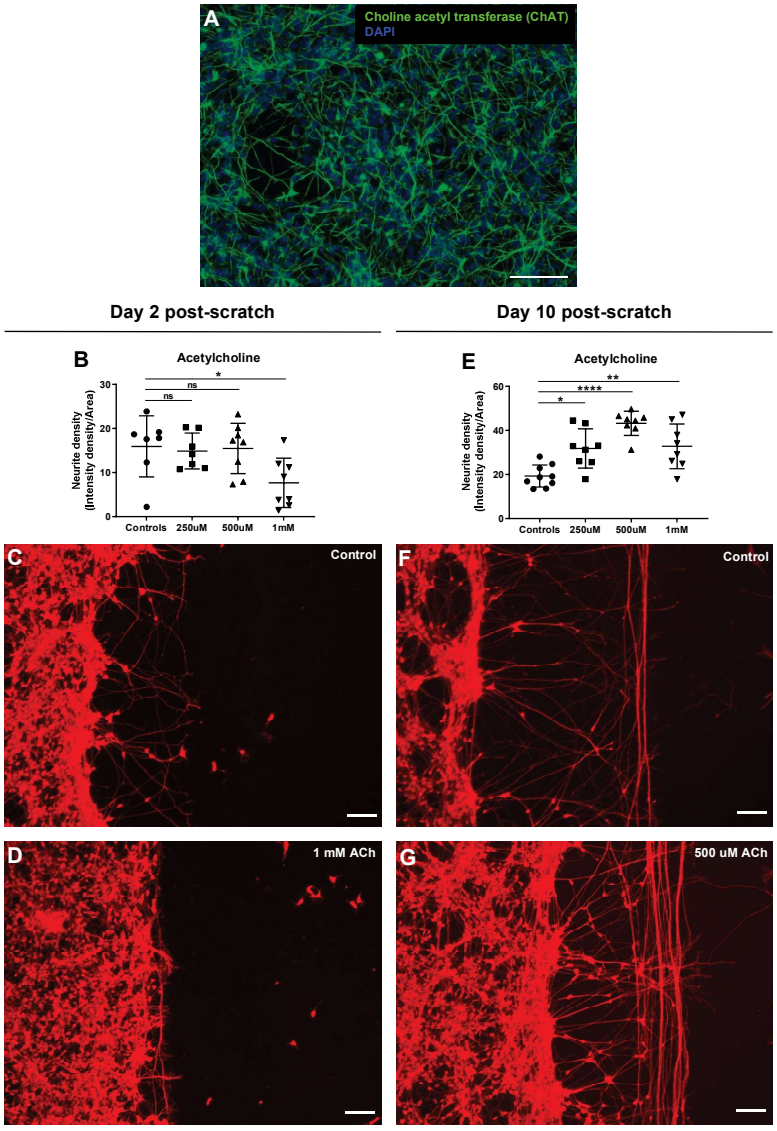

Figure 5: Acetylcholine shows biphasic effect on neurite outgrowth in scratch assay
(A) hiNSC derived day 10 mature neuronal culture show presence of cholinergic neurons (choline acetyl transferase marker). (B) Acetylcholine treatment (48 hours) shows a significant concentration dependent decline in scratch neurite density on day 2 post-scratch. (C-D) Representative images of Calcein Red-Orange AM stained control neural cultures (C) and neural cultures treated with 1 mM acetylcholine (D) on day 2 post-scratch showing diminished neurite outgrowths with acetylcholine treatment. (E) Acetylcholine treatment (48 hours) shows a significant concentration dependent increase in scratch neurite density on day 10 post-scratch. (F-G) Representative images of Calcein Red-Orange AM stained control neural cultures (F) and neural cultures treated with 500 µM acetylcholine (G) on day 10 post-scratch showing increased neurite outgrowth with acetylcholine treatment. All data are represented as mean±S.D. All scale bars, 100 µm.

Serotonin significantly enhances neurite outgrowth after scratch wound.

To test the effect of serotonin on neurite outgrowths after wounding, we first checked if hiNSC derived mature neurons have serotonergic neurons. Immunostaining for serotonin reuptake transporter showed bundles of serotonergic neurons within cultures (Figure 6A). Neurons were then mechanically wounded as mentioned above and left untreated (controls) or treated with three different concentrations of serotonin

Preprints (www.preprints.org) | NOT PEER-REVIEWED | Posted: 6 July 2022 doi:10.20944/preprints202207.0083.v1

(250µM, 500µM, 1mM) for 2 days. On day 2 post-scratch the 250µM serotonin treated scratch wounds were indistinguishable from controls (Figure 6B). However, 500µM and 1mM serotonin significantly increased the number of neurite outgrowth and neurite density (Figure 6B-D). Analogously, day 10-post-scratch showed a significant dose dependent increase (in comparison to controls) in overall neurite density in serotonin treatment (Figure 6E-G). The increase in neurite outgrowth is very striking (Figure 6F & G), with much longer neurite outgrowths (perpendicular to scratch surface) and very few fibers parallel to the scratch surface. Such extensive neurite outgrowth pattern is known to be conducive for nerve regeneration and wound healing [45,50-54,112,122]. Thus, serotonin exposure significantly enhances neurite outgrowths and serotonin treatment may aid in nerve and wound repair.

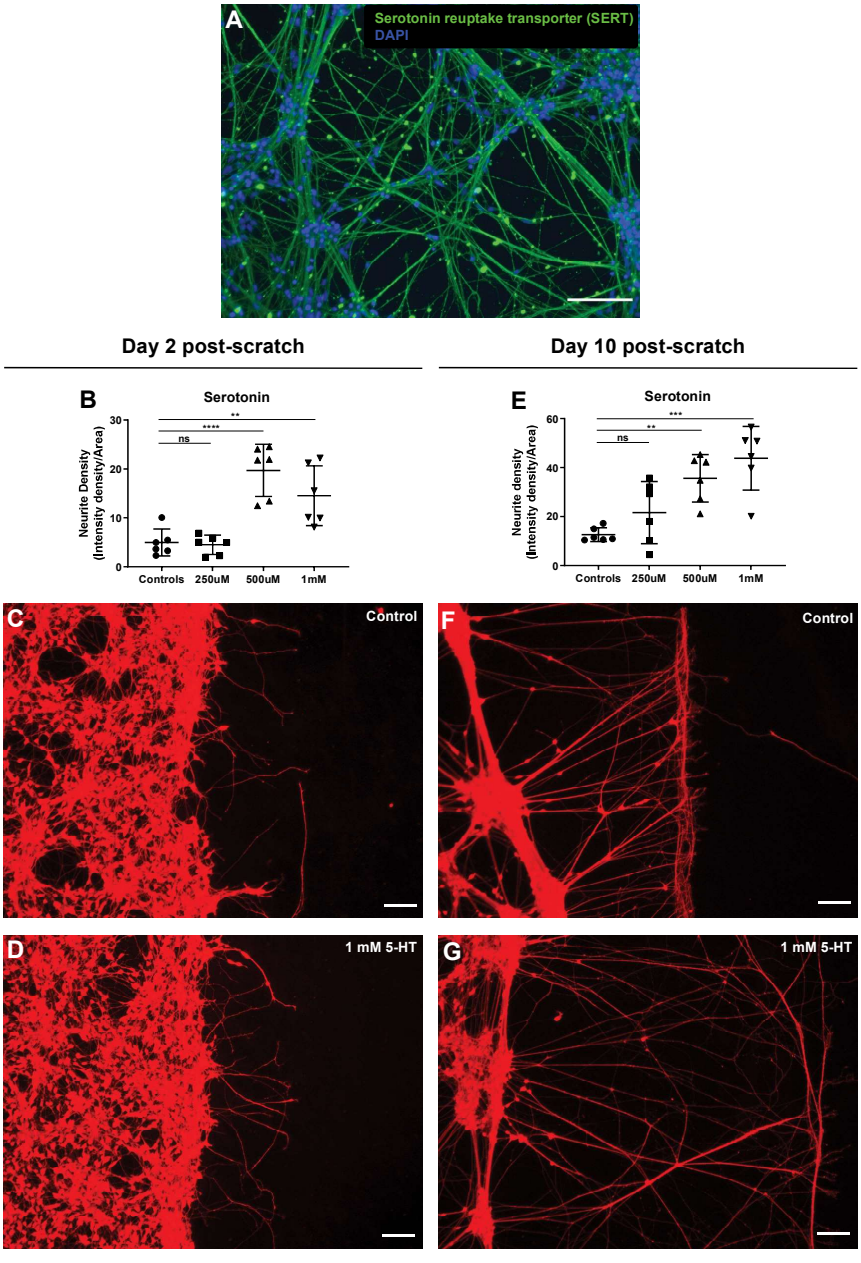

Preprints (www.preprints.org) | NOT PEER-REVIEWED | Posted: 6 July 2022 doi:10.20944/preprints202207.0083.v1

Figure 6: Serotonin significantly increases neurite outgrowth in scratch assay
(A) hiNSC derived day 10 mature neuronal culture show presence of serotonergic neurons (serotonin reuptake transporter marker). (B) Serotonin treatment (48 hours) shows a significant concentration dependent increase in scratch neurite density on day 2 post-scratch. (C-D) Representative images of Calcein Red-Orange AM stained control neural cultures (C) and neural cultures treated with 1 mM serotonin (D) on day 2 post-scratch showing increased neurite outgrowths with serotonin treatment. (E) Serotonin treatment (48 hours) shows a significant concentration dependent increase in scratch neurite density on day 10 post-scratch. (F-G) Representative images of Calcein Red-Orange AM stained control neural cultures (F) and neural cultures treated with 1 mM serotonin (G) on day 10 post-scratch showing increased neurite outgrowth with serotonin treatment. All data are represented as mean±S.D. All scale bars, 100 µm.

GABA has no effect on neurite outgrowth after scratch wound.

To test the effect of GABA on neurite outgrowths after wounding, we first checked if hiNSC derived mature neurons have GABAergic neurons. Immunostaining for glutamate decarboxylase showed GABAergic neurons within cultures (Figure 7A). Neurons were then mechanically wounded as mentioned above and left untreated (controls) or treated with three different concentrations of GABA (250µM, 500µM, 1mM) for 2 days. Both on day 2 post-scratch and day 10 post-scratch there was no discernable effect of GABA at any of the concentrations tested (Figure 7B-G). The neurite outgrowth density and patterns were indistinguishable from controls. Thus, although GABAergic neurons are present in culture, targeting them using GABA does not affect the neurite outgrowths and hence nerve and wound repair. However, loss-of-function (blockade) of native GABA signaling could be a target in future studies.

Preprints (www.preprints.org) | NOT PEER-REVIEWED | Posted: 6 July 2022 doi:10.20944/preprints202207.0083.v1

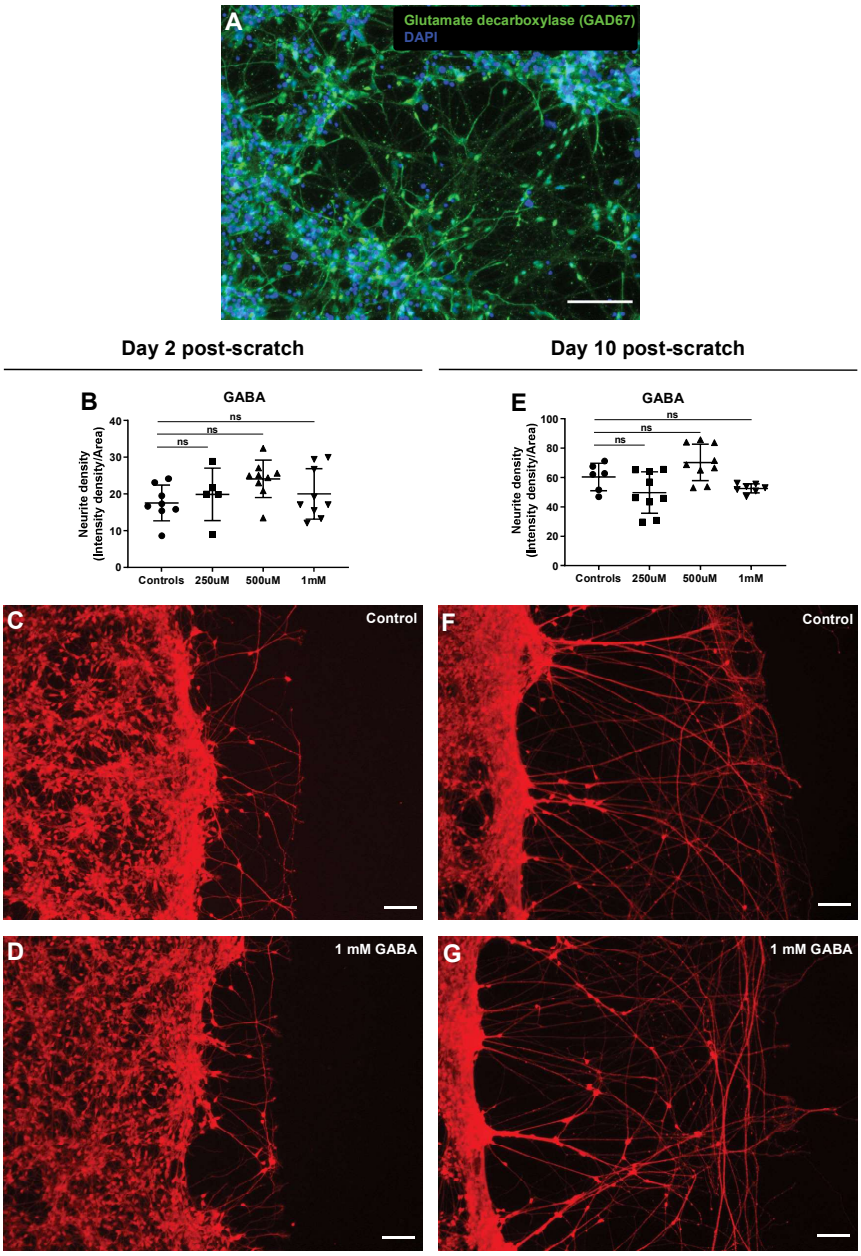

Figure 7: GABA does not affect neurite outgrowth in scratch assay
(A) hiNSC derived day 10 mature neuronal culture show presence of GABAergic neurons (glutamate decarboxylase – GAD67 marker). (B) GABA treatment (48 hours) shows no significant change in scratch neurite density on day 2 post-scratch. (C-D) Representative images of Calcein Red-Orange AM stained control neural cultures (C) and neural cultures treated with 1 mM GABA (D) on day 2 post-scratch showing no discernable change in neurite outgrowths with GABA treatment. (E) GABA treatment (48 hours) shows no significant change in scratch neurite density on day 10 post-scratch. (F-G) Representative images of Calcein Red-Orange AM stained control neural cultures (F) and neural cultures treated with 1 mM GABA (G) on day 10 post-scratch showing no discernable change in neurite outgrowth with GABA treatment. All data are represented as mean±S.D. All scale bars, 100 µm.

Extracellular pH change has biphasic effect on neurite outgrowth after scratch wound

Wound environments in general have elevated pH which is detrimental to wound healing and acidic pH has been shown to promote wound healing by various means such as altering protease activity, enhancing

Preprints (www.preprints.org) | NOT PEER-REVIEWED | Posted: 6 July 2022 doi:10.20944/preprints202207.0083.v1

epithelialization and angiogenesis [104-107]. To test the effect of pH on nerve and wound repair, hiNSC derived mature neurons were mechanically wounded as mentioned above and left untreated (controls) or incubated in regular culture media with pH adjusted to pH 6, 7, and 8 for 2 days. On day 2 post-scratch, neurons in pH7 and pH8 media had scratch wounds indistinguishable from controls (pH7.4) (Figure 8A). However, neurons in acidic pH6 media showed significantly higher neurite density (Figure 8A-C). However, the increase in neurite outgrowth pattern was mainly in form of increased fibers parallel to the scratch surface which is characteristic of detrimental nerve and wound repair (Figure 8C). In contrast, on day 10 post-scratch neurons exposed to pH6 media were not different from controls (pH7.4), however neurons exposed to both pH7 and pH8 showed significant decrease in neurite density and outgrowth (Figure 8D-F). Thus overall, it seems that elevated pH is detrimental for nerve and wound repair. This is in line with studies [104-107] showing that acidic wound environment promotes better wound healing. Thus, modulation of wound pH could be used as a strategy to boost nerve and in turn wound repair.

Here, we characterize a number of reagents that allow dynamic monitoring of cell morphology, membrane voltage, ion levels, and cell activity such as pH and reactive oxygen species, track responses to wounding and reinnervation, and show in a quantitative manner the ability of bioelectrical actuators (neurotransmitters and pH) to manipulate nerve wound re-innervation. Although our neurite scratch density measurements were very successful in detecting and quantifying changes in neurite outgrowths, they did not seem to capture the differences in patterns of neurite outgrowth. Hence additional quantitative measures such as computing neurite length and direction might have to be added for capturing the changes in patterns of neurite outgrowths [122,123]. Ultimately, these hiNSCs derived neurons can be co-cultured with glia, astrocytes, oligodendrocytes or with muscles, skin cells etc. [65,66] to further study the bioelectric and neurotransmitter signaling during complex interactions of these cells under various stimuli and experimental conditions. Future work on the biophysics of cultured stem cells will continue to enrich efforts to decipher the workings of cellular collectives during wound healing, regeneration and other environmental challenges, with many biomedical applications.

Preprints (www.preprints.org) | NOT PEER-REVIEWED | Posted: 6 July 2022 doi:10.20944/preprints202207.0083.v1

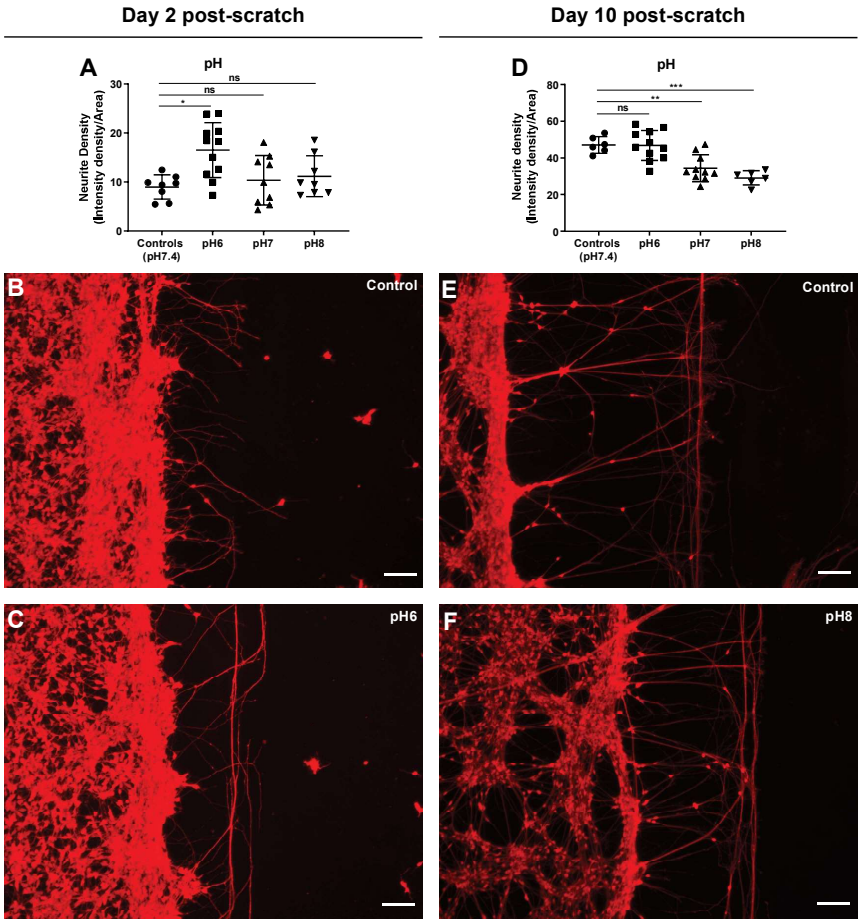

Figure 8: Extracellular pH change has biphasic effect on neurite outgrowth in scratch assay
(A) Extracellular pH change (48 hours) shows a significant increase in scratch neurite density at pH6 but no change at pH8 on day 2 post-scratch. (B-C) Representative images of Calcein Red-Orange AM stained control neural cultures (B) and neural cultures with extracellular pH6 (C) on day 2 post-scratch showing increased neurite outgrowths with pH6. (D) Extracellular pH change (48 hours) shows a significant decrease in scratch neurite density at both pH7 and pH8 but no change in pH6 on day 10 post-scratch. (E-F) Representative images of Calcein Red-Orange AM stained control neural cultures (E) and neural cultures treated with extracellular pH8 (F) on day 10 post-scratch showing decreased neurite outgrowth with pH8. All data are represented as mean±S.D. All scale bars, 100 µm.

Acknowledgements

We thank Rakela Colon for general lab assistance, David Kaplan for the generous gift of hiNSC cells.

Funding:

We gratefully acknowledge support of the Allen Discovery Center program through The Paul G. Allen Frontiers Group (12171), and the Defense Advanced Research Projects Agency (DARPA), Army Research Office, under Cooperative Agreement No. W911NF-18-2-0104, and the Department of Interior, Award No. D20AC00003.

Preprints (www.preprints.org) | NOT PEER-REVIEWED | Posted: 6 July 2022 doi:10.20944/preprints202207.0083.v1

Author contributions

V.P.P. and B.C. performed experiments, V.P.P., B.C., and M.L. designed the experiments and interpreted data. V.P.P. and M.L. wrote the manuscript together.

Competing Financial Interests

The authors declare no competing financial interests.

Supplemental material legends

Figure S1: NeuO stains non-neural M0 macrophage cells
THP-1 derived M0 macrophage cells stained with NeuO (green) showing live cell body and Hoechst (blue) showing nuclei. Scale bars, 100 µm.

Figure S2: MQAE live stain fail to label hiNSC derived mature neurons
hiNSC derived day 10 mature neurons stained with MQAE an intracellular Cl^- ion reporter. Scale bars, 100 µm.

Movie S1: hiNSC derived day 10 mature neurons stained with Fluo4 AM showing baseline Ca^{2+} dynamics in neurons

Table S1: Ionic composition (in mM) of extracellular solutions with changing Na^+ ion concentration and physiological levels in green. Adapted from [85]

NaCl	KCl	$CaCl_2$	$MaCl_2$	NMDG-Cl	HEPES	Glucose
28	5.4	1.8	1	112	10	5.5
56	5.4	1.8	1	84	10	5.5
84	5.4	1.8	1	56	10	5.5
112	5.4	1.8	1	28	10	5.5
140	5.4	1.8	1	0	10	5.5

Na^+	K^+	$NMDG^+$	Cl^-
28	5.4	112	151
56	5.4	84	151
84	5.4	56	151
112	5.4	28	151
140	5.4	0	151

Table S2: Ionic composition (in mM) of extracellular solutions with changing K^+ ion concentration and physiological levels in green. Adapted from [85]

NaCl	KCl	$CaCl_2$	$MaCl_2$	NMDG-Cl	HEPES	Glucose
0	5.4	1.8	1	140	10	5.5
0	35.4	1.8	1	110	10	5.5
0	65.4	1.8	1	80	10	5.5
0	100.4	1.8	1	45	10	5.5
0	135.4	1.8	1	10	10	5.5

Na^+	K^+	$NMDG^+$	Cl^-
0	5.4	140	151
0	35.4	110	151
0	65.4	80	151
0	100.4	45	151
0	135.4	10	151

Table S3: Ionic composition (in mM) of extracellular solutions within changing Na^+ and K^+ ion concentration for generating various resting membrane potentials with physiological levels in green. Adapted from [85]

NaCl	KCl	$CaCl_2$	$MaCl_2$	NMDG-Cl	HEPES	Glucose
140	5.4	1.8	1	0	10	5.5
110	35.4	1.8	1	0	10	5.5
80	65.4	1.8	1	0	10	5.5
45	100.4	1.8	1	0	0	5.5
10	135.4	1.8	1	0	0	5.5

Na^+	K^+	$NMDG^+$	Cl^-
140	5.4	0	151
110	35.4	0	151
80	65.4	0	151
45	100.4	0	151
10	135.4	0	151

Preprints (www.preprints.org) | NOT PEER-REVIEWED | Posted: 6 July 2022 doi:10.20944/preprints202207.0083.v1

References:

1. Levin, M.; Pezzulo, G.; Finkelstein, J.M. Endogenous Bioelectric Signaling Networks: Exploiting Voltage Gradients for Control of Growth and Form. *Annu Rev Biomed Eng* **2017**, *19*, 353-387, doi:10.1146/annurev-bioeng-071114-040647.
2. Nuccitelli, R. Endogenous electric fields in embryos during development, regeneration and wound healing. *Radiat Prot Dosimetry* **2003**, *106*, 375-383.
3. McCaig, C.D.; Song, B.; Rajnicek, A.M. Electrical dimensions in cell science. *J Cell Sci* **2009**, *122*, 4267-4276.
4. Humphries, J.; Xiong, L.; Liu, J.; Prindle, A.; Yuan, F.; Arjes, H.A.; Tsimring, L.; Suel, G.M. Species-Independent Attraction to Biofilms through Electrical Signaling. *Cell* **2017**, *168*, 200-209 e212, doi:10.1016/j.cell.2016.12.014.
5. Levin, M.; Martyniuk, C.J. The bioelectric code: An ancient computational medium for dynamic control of growth and form. *Biosystems* **2018**, *164*, 76-93, doi:10.1016/j.biosystems.2017.08.009.
6. Bates, E. Ion Channels in Development and Cancer. *Annu Rev Cell Dev Biol* **2015**, *31*, 231-247, doi:10.1146/annurev-cellbio-100814-125338.
7. Harris, M.P. Bioelectric signaling as a unique regulator of development and regeneration. *Development* **2021**, *148*, doi:10.1242/dev.180794.
8. Zebelo, S.A.; Matsui, K.; Ozawa, R.; Maffei, M.E. Plasma membrane potential depolarization and cytosolic calcium flux are early events involved in tomato (Solanum lycopersicon) plant-to-plant communication. *Plant Sci* **2012**, *196*, 93-100, doi:10.1016/j.plantsci.2012.08.006.
9. Christmann, A.; Grill, E. Plant biology: Electric defence. *Nature* **2013**, *500*, 404-405, doi:10.1038/500404a.
10. Levin, M. Bioelectric signaling: Reprogrammable circuits underlying embryogenesis, regeneration, and cancer. *Cell* **2021**, *184*, 1971-1989, doi:10.1016/j.cell.2021.02.034.
11. Stanger, B.Z. Organ size determination and the limits of regulation. *Cell Cycle* **2008**, *7*, 318-324.
12. Thompson, D. *On Growith and Form*; Cambridge University Press: Cambridge, England, 1942.
13. Harvey, K.F.; Hariharan, I.K. The hippo pathway. *Cold Spring Harb Perspect Biol* **2012**, *4*, a011288, doi:10.1101/cshperspect.a011288a011288 [pii]cshperspect.a011288 [pii].
14. Zhao, B.; Tumaneng, K.; Guan, K.L. The Hippo pathway in organ size control, tissue regeneration and stem cell self-renewal. *Nat Cell Biol* **2011**, *13*, 877-883, doi:10.1038/ncb2303ncb2303 [pii].
15. Pai, V.P.; Lemire, J.M.; Pare, J.F.; Lin, G.; Chen, Y.; Levin, M. Endogenous Gradients of Resting Potential Instructively Pattern Embryonic Neural Tissue via Notch Signaling and Regulation of Proliferation. *J Neurosci* **2015**, *35*, 4366-4385, doi:10.1523/JNEUROSCI.1877-14.2015.
16. Pai, V.P.; Aw, S.; Shomrat, T.; Lemire, J.M.; Levin, M. Transmembrane voltage potential controls embryonic eye patterning in Xenopus laevis. *Development* **2012**, *139*, 313-323, doi:10.1242/dev.073759.
17. Chu, C.W.; Masak, G.; Yang, J.; Davidson, L.A. From biomechanics to mechanobiology: Xenopus provides direct access to the physical principles that shape the embryo. *Curr Opin Genet Dev* **2020**, *63*, 71-77, doi:10.1016/j.gde.2020.05.011.
18. Davidson, L.A. Mechanical design in embryos: mechanical signalling, robustness and developmental defects. *Philos Trans R Soc Lond B Biol Sci* **2017**, *372*, doi:10.1098/rstb.2015.0516.
19. Boulan, L.; Leopold, P. What determines organ size during development and regeneration? *Development* **2021**, *148*, doi:10.1242/dev.196063.
20. McCaig, C.D.; Rajnicek, A.M.; Song, B.; Zhao, M. Controlling cell behavior electrically: current views and future potential. *Physiol Rev* **2005**, *85*, 943-978.
21. Pai, V.P.; Levin, M. HCN2 Channel-induced Rescue of Brain, Eye, Heart, and Gut Teratogenesis Caused by Nicotine, Ethanol, and Aberrant Notch Signaling. *Wound Repair Regen* **2022**, doi:10.1111/wrr.13032.
22. Pai, V.P.; Pietak, A.; Willocq, V.; Ye, B.; Shi, N.Q.; Levin, M. HCN2 Rescues brain defects by enforcing endogenous voltage pre-patterns. *Nat Commun* **2018**, *9*, 998, doi:10.1038/s41467-018-03334-5.
23. Pai, V.P.; Cervera, J.; Mafe, S.; Willocq, V.; Lederer, E.K.; Levin, M. HCN2 Channel-Induced Rescue of Brain Teratogenesis via Local and Long-Range Bioelectric Repair. *Front Cell Neurosci* **2020**, *14*, 136, doi:10.3389/fncel.2020.00136.

Preprints (www.preprints.org) | NOT PEER-REVIEWED | Posted: 6 July 2022 doi:10.20944/preprints202207.0083.v1

24. Churchill, C.D.M.; Winter, P.; Tuszynski, J.A.; Levin, M. EDEn-Electroceutical Design Environment: Ion Channel Tissue Expression Database with Small Molecule Modulators. *iScience* **2019**, *11*, 42-56, doi:10.1016/j.isci.2018.12.003.
25. Guo, S.; Dipietro, L.A. Factors affecting wound healing. *J Dent Res* **2010**, *89*, 219-229, doi:10.1177/0022034509359125.
26. Gurtner, G.C.; Werner, S.; Barrandon, Y.; Longaker, M.T. Wound repair and regeneration. *Nature* **2008**, *453*, 314-321, doi:10.1038/nature07039.
27. Durant, F.; Whited, J.L. Finding Solutions for Fibrosis: Understanding the Innate Mechanisms Used by Super-Regenerator Vertebrates to Combat Scarring. *Adv Sci (Weinh)* **2021**, *8*, e2100407, doi:10.1002/advs.202100407.
28. Slater, P.G.; Palacios, M.; Larrain, J. Xenopus, a Model to Study Wound Healing and Regeneration: Experimental Approaches. *Cold Spring Harb Protoc* **2021**, *2021*, doi:10.1101/pdb.top100966.
29. Kaliya-Perumal, A.K.; Ingham, P.W. Musculoskeletal regeneration: A zebrafish perspective. *Biochimie* **2022**, *196*, 171-181, doi:10.1016/j.biochi.2021.10.014.
30. Chifflet, S.; Hernandez, J.A. The Epithelial Sodium Channel and the Processes of Wound Healing. *Biomed Res Int* **2016**, *2016*, 5675047, doi:10.1155/2016/5675047.
31. Franklin, B.M.; Voss, S.R.; Osborn, J.L. Ion channel signaling influences cellular proliferation and phagocyte activity during axolotl tail regeneration. *Mech Dev* **2017**, *146*, 42-54, doi:10.1016/j.mod.2017.06.001.
32. Zhang, W.; Das, P.; Kelangi, S.; Bei, M. Potassium channels as potential drug targets for limb wound repair and regeneration. *Precis Clin Med* **2020**, *3*, 22-33, doi:10.1093/pcmedi/pbz029.
33. Reid, B.; Zhao, M. The Electrical Response to Injury: Molecular Mechanisms and Wound Healing. *Adv Wound Care (New Rochelle)* **2014**, *3*, 184-201, doi:10.1089/wound.2013.0442.
34. Chifflet, S.; Hernandez, J.A.; Grasso, S. A possible role for membrane depolarization in epithelial wound healing. *Am J Physiol Cell Physiol* **2005**, *288*, C1420-1430, doi:10.1152/ajpcell.00259.2004.
35. Messerli, M.A.; Graham, D.M. Extracellular electrical fields direct wound healing and regeneration. *Biol. Bull.* **2011**, *221*, 79-92, doi:10.1086/BBLv221n1p79.
36. Zhao, M. Electrical fields in wound healing-An overriding signal that directs cell migration. *Semin Cell Dev Biol* **2009**, *20*, 674-682.
37. Sundelacruz, S.; Li, C.; Choi, Y.J.; Levin, M.; Kaplan, D.L. Bioelectric modulation of wound healing in a 3D in vitro model of tissue-engineered bone. *Biomaterials* **2013**, *34*, 6695-6705, doi:S0142-9612(13)00616-9 [pii] 10.1016/j.biomaterials.2013.05.040.
38. Zhang, W.; Bei, M. Kcnh2 and Kcnj8 interactively regulate skin wound healing and regeneration. *Wound Repair Regen* **2015**, *23*, 797-806, doi:10.1111/wrr.12347.
39. Richard B. Borgens, K.R.R., Joseph W. Vanable, Jr., and Michael E. McGinnis, with Colin D. McCaig. *Electric Fields in Vertebrate Repair: Natural and Applied Voltages in Vertebrate Regeneration and Healing*; Wiley-Liss: New York, 1989.
40. Pai, V.P.; Levin, M. Chapter 5: Bioelectric Control of Stem Cell Function. In *Stem Cells: From Basic Research to Therapy*, Calegari, F., Waskov, C., Eds.; Science Publisher: 2014; Volume 1, pp. 106-148.
41. Adams, D.S.; Masi, A.; Levin, M. H+ pump-dependent changes in membrane voltage are an early mechanism necessary and sufficient to induce Xenopus tail regeneration. *Development* **2007**, *134*, 1323-1335, doi:10.1242/dev.02812.
42. Tseng, A.S.; Levin, M. Transducing bioelectric signals into epigenetic pathways during tadpole tail regeneration. *Anat Rec (Hoboken)* **2012**, *295*, 1541-1551, doi:10.1002/ar.22495.
43. Perathoner, S.; Daane, J.M.; Henrion, U.; Seebohm, G.; Higdon, C.W.; Johnson, S.L.; Nusslein-Volhard, C.; Harris, M.P. Bioelectric signaling regulates size in zebrafish fins. *PLoS genetics* **2014**, *10*, e1004080, doi:10.1371/journal.pgen.1004080.
44. Nuccitelli, R. A role for endogenous electric fields in wound healing. *Curr Top Dev Biol* **2003**, *58*, 1-26.
45. Singer, M. The influence of the nerve in regeneration of the amphibian extremity. *Q Rev Biol* **1952**, *27*, 169-200.
46. Mitogawa, K.; Makanae, A.; Satoh, A. Hyperinnervation improves Xenopus laevis limb regeneration. *Dev Biol* **2018**, *433*, 276-286, doi:10.1016/j.ydbio.2017.10.007.

Preprints (www.preprints.org) | NOT PEER-REVIEWED | Posted: 6 July 2022 doi:10.20944/preprints202207.0083.v1

47. Nieto-Diaz, M.; Pita-Thomas, D.W.; Munoz-Galdeano, T.; Martinez-Maza, C.; Navarro-Ruiz, R.; Reigada, D.; Yunta, M.; Caballero-Lopez, M.J.; Nieto-Sampedro, M.; Martinez-Maza, R. Deer antler innervation and regeneration. *Front Biosci (Landmark Ed)* **2012**, *17*, 1389-1401, doi:10.2741/3993.
48. Filoni, S.; Velloso, C.P.; Bernardini, S.; Cannata, S.M. Acquisition of nerve dependence for the formation of a regeneration blastema in amputated hindlimbs of larval Xenopus laevis: the role of limb innervation and that of limb differentiation. *J Exp Zool* **1995**, *273*, 327-341.
49. Wislocki, G.B.; Singer, M. The occurrence and function of nerves in the growing antlers of deer. *J Comp Neurol* **1946**, *85*, 1-19, doi:10.1002/cne.900850102.
50. Kumar, A.; Brockes, J.P. Nerve dependence in tissue, organ, and appendage regeneration. *Trends Neurosci* **2012**, *35*, 691-699, doi:10.1016/j.tins.2012.08.003.
51. Ge, S.; Khachemoune, A. The Importance of Cutaneous Innervation in Wound Healing: From Animal Studies to Clinical Applications. *Int J Low Extrem Wounds* **2021**, 15347346211045022, doi:10.1177/15347346211045022.
52. Knox, S.M.; Lombaert, I.M.; Haddox, C.L.; Abrams, S.R.; Cotrim, A.; Wilson, A.J.; Hoffman, M.P. Parasympathetic stimulation improves epithelial organ regeneration. *Nat Commun* **2013**, *4*, 1494, doi:10.1038/ncomms2493.
53. Ashrafi, M.; Baguneid, M.; Bayat, A. The Role of Neuromediators and Innervation in Cutaneous Wound Healing. *Acta Derm Venereol* **2016**, *96*, 587-594, doi:10.2340/00015555-2321.
54. Emmerson, E. Efficient Healing Takes Some Nerve: Electrical Stimulation Enhances Innervation in Cutaneous Human Wounds. *J Invest Dermatol* **2017**, *137*, 543-545, doi:10.1016/j.jid.2016.10.018.
55. Carlson, B.M. Some principles of regeneration in mammalian systems. *Anat Rec B New Anat* **2005**, *287*, 4-13, doi:10.1002/ar.b.20079.
56. Wu, C.L.; Chou, Y.H.; Chang, Y.J.; Teng, N.Y.; Hsu, H.L.; Chen, L. Interplay between cell migration and neurite outgrowth determines SH2B1beta-enhanced neurite regeneration of differentiated PC12 cells. *PLoS One* **2012**, *7*, e34999, doi:10.1371/journal.pone.0034999.
57. Cao, L.; Wei, D.; Reid, B.; Zhao, S.; Pu, J.; Pan, T.; Yamoah, E.; Zhao, M. Endogenous electric currents might guide rostral migration of neuroblasts. *EMBO Rep* **2013**, *14*, 184-190, doi:10.1038/embor.2012.215embor2012215 [pii].
58. Jaffe, L.F.; Poo, M.M. Neurites grow faster towards the cathode than the anode in a steady field. *J Exp Zool* **1979**, *209*, 115-128, doi:10.1002/jez.1402090114.
59. Song, B.; Zhao, M.; Forrester, J.; McCaig, C. Nerve regeneration and wound healing are stimulated and directed by an endogenous electrical field in vivo. *J Cell Sci* **2004**, *117*, 4681-4690, doi:10.1242/jcs.01341
60. Breier, J.M.; Radio, N.M.; Mundy, W.R.; Shafer, T.J. Development of a high-throughput screening assay for chemical effects on proliferation and viability of immortalized human neural progenitor cells. *Toxicol Sci* **2008**, *105*, 119-133, doi:10.1093/toxsci/kfn115.
61. Radio, N.M.; Breier, J.M.; Shafer, T.J.; Mundy, W.R. Assessment of chemical effects on neurite outgrowth in PC12 cells using high content screening. *Toxicol Sci* **2008**, *105*, 106-118, doi:10.1093/toxsci/kfn114.
62. Young, A.; Machacek, D.W.; Dhara, S.K.; Macleish, P.R.; Benveniste, M.; Dodla, M.C.; Sturkie, C.D.; Stice, S.L. Ion channels and ionotropic receptors in human embryonic stem cell derived neural progenitors. *Neuroscience* **2011**, *192*, 793-805, doi:10.1016/j.neuroscience.2011.04.039.
63. Dragunow, M. High-content analysis in neuroscience. *Nat Rev Neurosci* **2008**, *9*, 779-788, doi:10.1038/nrn2492.
64. Harrill, J.A.; Robinette, B.L.; Freudenrich, T.; Mundy, W.R. Use of high content image analyses to detect chemical-mediated effects on neurite sub-populations in primary rat cortical neurons. *Neurotoxicology* **2013**, *34*, 61-73, doi:10.1016/j.neuro.2012.10.013.
65. Cairns, D.M.; Chwalek, K.; Moore, Y.E.; Kelley, M.R.; Abbott, R.D.; Moss, S.; Kaplan, D.L. Expandable and Rapidly Differentiating Human Induced Neural Stem Cell Lines for Multiple Tissue Engineering Applications. *Stem Cell Reports* **2016**, *7*, 557-570, doi:10.1016/j.stemcr.2016.07.017.
66. Cairns, D.M.; Giordano, J.E.; Conte, S.; Levin, M.; Kaplan, D.L. Ivermectin Promotes Peripheral Nerve Regeneration during Wound Healing. *ACS Omega* **2018**, *3*, 12392-12402, doi:10.1021/acsomega.8b01451.
67. Hu, B.Y.; Weick, J.P.; Yu, J.; Ma, L.X.; Zhang, X.Q.; Thomson, J.A.; Zhang, S.C. Neural differentiation of human induced pluripotent stem cells follows developmental principles but with variable potency. *Proc Natl Acad Sci U S A* **2010**, *107*, 4335-4340, doi:10.1073/pnas.0910012107.

Preprints (www.preprints.org) | NOT PEER-REVIEWED | Posted: 6 July 2022 doi:10.20944/preprints202207.0083.v1

68. Chen, G.; Gulbranson, D.R.; Hou, Z.; Bolin, J.M.; Ruotti, V.; Probasco, M.D.; Smuga-Otto, K.; Howden, S.E.; Diol, N.R.; Propson, N.E.; et al. Chemically defined conditions for human iPSC derivation and culture. *Nat Methods* **2011**, *8*, 424-429, doi:10.1038/nmeth.1593.
69. Efthymiou, A.; Shaltouki, A.; Steiner, J.P.; Jha, B.; Heman-Ackah, S.M.; Swistowski, A.; Zeng, X.; Rao, M.S.; Malik, N. Functional screening assays with neurons generated from pluripotent stem cell-derived neural stem cells. *J Biomol Screen* **2014**, *19*, 32-43, doi:10.1177/1087057113501869.
70. Rosati, J.; Ferrari, D.; Altieri, F.; Tardivo, S.; Ricciolini, C.; Fusilli, C.; Zalfa, C.; Profico, D.C.; Pinos, F.; Bernardini, L.; et al. Establishment of stable iPS-derived human neural stem cell lines suitable for cell therapies. *Cell Death Dis* **2018**, *9*, 937, doi:10.1038/s41419-018-0990-2.
71. Sirenko, O.; Hesley, J.; Rusyn, I.; Cromwell, E.F. High-content high-throughput assays for characterizing the viability and morphology of human iPSC-derived neuronal cultures. *Assay Drug Dev Technol* **2014**, *12*, 536-547, doi:10.1089/adt.2014.592.
72. Zhang, X.; Kiechle, F.L. Hoechst 33342-induced apoptosis in BC3H-1 myocytes. *Ann Clin Lab Sci* **1997**, *27*, 260-275.
73. Gilbert, D.F.; Erdmann, G.; Zhang, X.; Fritzsche, A.; Demir, K.; Jaedicke, A.; Muehlenberg, K.; Wanker, E.E.; Boutros, M. A novel multiplex cell viability assay for high-throughput RNAi screening. *PLoS One* **2011**, *6*, e28338, doi:10.1371/journal.pone.0028338.
74. Borodinsky, L.N.; Belgacem, Y.H. Crosstalk among electrical activity, trophic factors and morphogenetic proteins in the regulation of neurotransmitter phenotype specification. *J. Chem. Neuroanat.* **2016**, *73*, 3-8, doi:10.1016/j.jchemneu.2015.12.001.
75. Belgacem, Y.H.; Borodinsky, L.N. Inversion of Sonic hedgehog action on its canonical pathway by electrical activity. *Proc Natl Acad Sci U S A* **2015**, *112*, 4140-4145, doi:10.1073/pnas.1419690112.
76. Beane, W.S.; Morokuma, J.; Lemire, J.M.; Levin, M. Bioelectric signaling regulates head and organ size during planarian regeneration. *Development* **2013**, *140*, 313-322, doi:10.1242/dev.086900.
77. Pai, V.P.; Vandenberg, L.N.; Blackiston, D.; Levin, M. Neurally Derived Tissues in Xenopus laevis Embryos Exhibit a Consistent Bioelectrical Left-Right Asymmetry. *Stem Cells Int* **2012**, *2012*, 353491, doi:10.1155/2012/353491.
78. Pai, V.P.; Lemire, J.M.; Chen, Y.; Lin, G.; Levin, M. Local and long-range endogenous resting potential gradients antagonistically regulate apoptosis and proliferation in the embryonic CNS. *Int J Dev Biol* **2015**, *59*, 327-340, doi:10.1387/ijdb.150197ml.
79. Smith, R.S.; Kenny, C.J.; Ganesh, V.; Jang, A.; Borges-Monroy, R.; Partlow, J.N.; Hill, R.S.; Shin, T.; Chen, A.Y.; Doan, R.N.; et al. Sodium Channel SCN3A (NaV1.3) Regulation of Human Cerebral Cortical Folding and Oral Motor Development. *Neuron* **2018**, *99*, 905-913 e907, doi:10.1016/j.neuron.2018.07.052.
80. Sequerra, E.B.; Goyal, R.; Castro, P.A.; Levin, J.B.; Borodinsky, L.N. NMDA Receptor Signaling Is Important for Neural Tube Formation and for Preventing Antiepileptic Drug-Induced Neural Tube Defects. *J Neurosci* **2018**, *38*, 4762-4773, doi:10.1523/JNEUROSCI.2634-17.2018.
81. Aprea, J.; Calegari, F. Bioelectric state and cell cycle control of Mammalian neural stem cells. *Stem Cells Int* **2012**, *2012*, 816049, doi:10.1155/2012/816049.
82. Lange, C.; Prenninger, S.; Knuckles, P.; Taylor, V.; Levin, M.; Calegari, F. The H(+) vacuolar ATPase maintains neural stem cells in the developing mouse cortex. *Stem Cells Dev* **2011**, *20*, 843-850, doi:10.1089/scd.2010.0484.
83. Ribera, A.B. Potassium currents in developing neurons. *Ann N Y Acad Sci* **1999**, *868*, 399-405, doi:10.1111/j.1749-6632.1999.tb11301.x.
84. Meier, S.D.; Kovalchuk, Y.; Rose, C.R. Properties of the new fluorescent Na+ indicator CoroNa Green: comparison with SBFI and confocal Na+ imaging. *J Neurosci Methods* **2006**, *155*, 251-259, doi:10.1016/j.jneumeth.2006.01.009.
85. Bonzanni, M.; Payne, S.L.; Adelfio, M.; Kaplan, D.L.; Levin, M.; Oudin, M.J. Defined extracellular ionic solutions to study and manipulate the cellular resting membrane potential. *Biol Open* **2020**, *9*, doi:10.1242/bio.048553.
86. Rana, P.S.; Gibbons, B.A.; Vereninov, A.A.; Yurinskaya, V.E.; Clements, R.J.; Model, T.A.; Model, M.A. Calibration and characterization of intracellular Asante Potassium Green probes, APG-2 and APG-4. *Anal Biochem* **2019**, *567*, 8-13, doi:10.1016/j.ab.2018.11.024.
87. Funk, R. Ion Gradients in Tissue and Organ Biology. *Biological Systems* **2013**, doi:doi: 10.4172/bso.1000105.

Preprints (www.preprints.org) | NOT PEER-REVIEWED | Posted: 6 July 2022 doi:10.20944/preprints202207.0083.v1

88. Blackiston, D.; Adams, D.S.; Lemire, J.M.; Lobikin, M.; Levin, M. Transmembrane potential of GlyCl-expressing instructor cells induces a neoplastic-like conversion of melanocytes via a serotonergic pathway. *Disease models & mechanisms* **2011**, *4*, 67-85, doi:10.1242/dmm.005561.
89. Engels, M.; Kalia, M.; Rahmati, S.; Petersilie, L.; Kovermann, P.; van Putten, M.; Rose, C.R.; Meijer, H.G.E.; Gensch, T.; Fahlke, C. Glial Chloride Homeostasis Under Transient Ischemic Stress. *Front Cell Neurosci* **2021**, *15*, 735300, doi:10.3389/fncel.2021.735300.
90. Igarashi, K.; Iwai, H.; Tanaka, K.I.; Kuwahara, Y.; Kitanaka, J.; Kitanaka, N.; Kurimasa, A.; Tomita, K.; Sato, T. Neuroprotective effect of oxytocin on cognitive dysfunction, DNA damage, and intracellular chloride disturbance in young mice after cranial irradiation. *Biochem Biophys Res Commun* **2022**, *612*, 1-7, doi:10.1016/j.bbrc.2022.04.099.
91. Janach, G.M.S.; Bohm, M.; Dohne, N.; Kim, H.R.; Rosario, M.; Strauss, U. Interferon-gamma enhances neocortical synaptic inhibition by promoting membrane association and phosphorylation of GABAA receptors in a protein kinase C-dependent manner. *Brain Behav Immun* **2022**, *101*, 153-164, doi:10.1016/j.bbi.2022.01.001.
92. Yang, W.; Yuste, R. In vivo imaging of neural activity. *Nat Methods* **2017**, *14*, 349-359, doi:10.1038/nmeth.4230.
93. Wong, R.O. Effects of glutamate and its analogs on intracellular calcium levels in the developing retina. *Vis Neurosci* **1995**, *12*, 907-917, doi:10.1017/s0952523800009469.
94. Rajdev, S.; Reynolds, I.J. Glutamate-induced intracellular calcium changes and neurotoxicity in cortical neurons in vitro: effect of chemical ischemia. *Neuroscience* **1994**, *62*, 667-679, doi:10.1016/0306-4522(94)90468-5.
95. McMillen, P.; Novak, R.; Levin, M. Toward Decoding Bioelectric Events in Xenopus Embryogenesis: New Methodology for Tracking Interplay Between Calcium and Resting Potentials In Vivo. *J Mol Biol* **2020**, *432*, 605-620, doi:10.1016/j.jmb.2019.10.029.
96. Sundelacruz, S.; Levin, M.; Kaplan, D.L. Role of membrane potential in the regulation of cell proliferation and differentiation. *Stem Cell Rev* **2009**, *5*, 231-246, doi:10.1007/s12015-009-9080-2.
97. Lagache, T.; Hanson, A.; Perez-Ortega, J.E.; Fairhall, A.; Yuste, R. Tracking calcium dynamics from individual neurons in behaving animals. *PLoS Comput Biol* **2021**, *17*, e1009432, doi:10.1371/journal.pcbi.1009432.
98. Dolensek, J.; Stozer, A.; Skelin Klemen, M.; Miller, E.W.; Slak Rupnik, M. The relationship between membrane potential and calcium dynamics in glucose-stimulated beta cell syncytium in acute mouse pancreas tissue slices. *PLoS One* **2013**, *8*, e82374, doi:10.1371/journal.pone.0082374.
99. Brodskiy, P.A.; Zartman, J.J. Calcium as a signal integrator in developing epithelial tissues. *Phys Biol* **2018**, *15*.
100. Adams, D.S.; Levin, M. Measuring resting membrane potential using the fluorescent voltage reporters DiBAC4(3) and CC2-DMPE. *Cold Spring Harb Protoc* **2012**, *2012*, 459-464, doi:10.1101/pdb.prot067702.
101. Oviedo, N.J.; Nicolas, C.L.; Adams, D.S.; Levin, M. Live Imaging of Planarian Membrane Potential Using DiBAC4(3). *CSH Protoc* **2008**, *2008*, pdb prot5055, doi:10.1101/pdb.prot5055.
102. Chesler, M. Regulation and modulation of pH in the brain. *Physiol Rev* **2003**, *83*, 1183-1221, doi:10.1152/physrev.00010.2003.
103. Ruffin, V.A.; Salameh, A.I.; Boron, W.F.; Parker, M.D. Intracellular pH regulation by acid-base transporters in mammalian neurons. *Front Physiol* **2014**, *5*, 43, doi:10.3389/fphys.2014.00043.
104. Jones, E.M.; Cochrane, C.A.; Percival, S.L. The Effect of pH on the Extracellular Matrix and Biofilms. *Adv Wound Care (New Rochelle)* **2015**, *4*, 431-439, doi:10.1089/wound.2014.0538.
105. Rodgers, A.; Watret, L. The role of pH modulation in wound bed preparation. *The Diabetic Foot* **2005**, *8*.
106. Bennison, L.R.; Miller, C.N.; Summers, R.J.; Minnis, A.M.B.; Sussman, G.; McGuiness, W. The pH of wounds during healing and infection: a descriptive literature review. *Wound Practice and Research* **2017**, *25*.
107. Percival, S.L.; McCarty, S.; Hunt, J.A.; Woods, E.J. The effects of pH on wound healing, biofilms, and antimicrobial efficacy. *Wound Repair Regen* **2014**, *22*, 174-186, doi:10.1111/wrr.12125.
108. Biswas, K.; Alexander, K.; Francis, M.M. Reactive Oxygen Species: Angels and Demons in the Life of a Neuron. *NeuroSci* **2022**, *3*, 130-145, doi:https://doi.org/10.3390/neurosci3010011.
109. Massaad, C.A.; Klann, E. Reactive oxygen species in the regulation of synaptic plasticity and memory. *Antioxid Redox Signal* **2011**, *14*, 2013-2054, doi:10.1089/ars.2010.3208.
110. Beckhauser, T.F.; Francis-Oliveira, J.; De Pasquale, R. Reactive Oxygen Species: Physiological and Physiopathological Effects on Synaptic Plasticity. *J Exp Neurosci* **2016**, *10*, 23-48, doi:10.4137/JEN.S39887.

Preprints (www.preprints.org) | NOT PEER-REVIEWED | Posted: 6 July 2022 doi:10.20944/preprints202207.0083.v1

111. Dickinson, B.C.; Huynh, C.; Chang, C.J. A palette of fluorescent probes with varying emission colors for imaging hydrogen peroxide signaling in living cells. *J Am Chem Soc* **2010**, *132*, 5906-5915, doi:10.1021/ja1014103.
112. Harsum, S.; Clarke, J.D.; Martin, P. A reciprocal relationship between cutaneous nerves and repairing skin wounds in the developing chick embryo. *Dev Biol* **2001**, *238*, 27-39, doi:10.1006/dbio.2001.0395 S0012-1606(01)90395-1 [pii].
113. Baig, A.M.; Rana, Z.; Tariq, S.; Lalani, S.; Ahmad, H.R. Traced on the Timeline: Discovery of Acetylcholine and the Components of the Human Cholinergic System in a Primitive Unicellular Eukaryote Acanthamoeba spp. *ACS Chem Neurosci* **2018**, *9*, 494-504, doi:10.1021/acschemneuro.7b00254.
114. Ramesh, S.A.; Tyerman, S.D.; Gilliham, M.; Xu, B. gamma-Aminobutyric acid (GABA) signalling in plants. *Cell Mol Life Sci* **2017**, *74*, 1577-1603, doi:10.1007/s00018-016-2415-7.
115. Erdo, S.L.; Wolff, J.R. gamma-Aminobutyric acid outside the mammalian brain. *J Neurochem* **1990**, *54*, 363-372, doi:10.1111/j.1471-4159.1990.tb01882.x.
116. Soltani, N.; Qiu, H.; Aleksic, M.; Glinka, Y.; Zhao, F.; Liu, R.; Li, Y.; Zhang, N.; Chakrabarti, R.; Ng, T.; et al. GABA exerts protective and regenerative effects on islet beta cells and reverses diabetes. *Proc Natl Acad Sci U S A* **2011**, *108*, 11692-11697, doi:10.1073/pnas.1102715108.
117. Tuszynski, J.; Tilli, T.M.; Levin, M. Ion Channel and Neurotransmitter Modulators as Electroceutical Approaches to the Control of Cancer. *Curr Pharm Des* **2017**, *23*, 4827-4841, doi:10.2174/1381612823666170530105837.
118. Blackiston, D.J.; Vien, K.; Levin, M. Serotonergic stimulation induces nerve growth and promotes visual learning via posterior eye grafts in a vertebrate model of induced sensory plasticity. *NPJ Regen Med* **2017**, *2*, 8, doi:10.1038/s41536-017-0012-5.
119. Fukumoto, T.; Kema, I.P.; Levin, M. Serotonin signaling is a very early step in patterning of the left-right axis in chick and frog embryos. *Curr Biol* **2005**, *15*, 794-803, doi:10.1016/j.cub.2005.03.044.
120. Halder, N.; Lal, G. Cholinergic System and Its Therapeutic Importance in Inflammation and Autoimmunity. *Front Immunol* **2021**, *12*, 660342, doi:10.3389/fimmu.2021.660342.
121. Maurer, S.V.; Williams, C.L. The Cholinergic System Modulates Memory and Hippocampal Plasticity via Its Interactions with Non-Neuronal Cells. *Front Immunol* **2017**, *8*, 1489, doi:10.3389/fimmu.2017.01489.
122. Stupack, J.; Xiong, X.P.; Jiang, L.L.; Zhang, T.; Zhou, L.; Campos, A.; Ranscht, B.; Mobley, W.; Pasquale, E.B.; Xu, H.; et al. Soluble SORLA Enhances Neurite Outgrowth and Regeneration through Activation of the EGF Receptor/ERK Signaling Axis. *J Neurosci* **2020**, *40*, 5908-5921, doi:10.1523/JNEUROSCI.0723-20.2020.
123. Pool, M.; Thiemann, J.; Bar-Or, A.; Fournier, A.E. NeuriteTracer: a novel ImageJ plugin for automated quantification of neurite outgrowth. *J Neurosci Methods* **2008**, *168*, 134-139, doi:10.1016/j.jneumeth.2007.08.029.